Noname manuscript No.
(will be inserted by the editor)

Local wind regime induced by giant linear dunes

Cyril Gadal · Pauline Delorme · Clément Narteau · Giles F.S. Wiggs · Matthew Baddock · Joanna M. Nield · Philippe Claudin

Received: DD Month YEAR / Accepted: DD Month YEAR

Abstract
Emergence and growth of sand dunes result from the interaction between the topography, which perturbs the wind flow, which itself controls the sediment transport. While these feedbacks are well studied at the scale of a single dune, the average effect of a periodic dune pattern on atmospheric flows remains poorly constrained due to a lack of data in major sand seas. Here, we compare field measurements of surface wind data to the predictions of the ERA5-Land climate reanalysis in four different places in Namibia, inside and north of the giant-dune field of the Namib sand sea. In the flat desert areas to the north, observations and predictions agree well despite the small amount of data in the assimilation process. This is also the case in the interdune areas of the sand sea, except for the weak winds blowing at night in a direction oblique to the

C. Gadal
Institut de Mécanique des Fluides de Toulouse, Université de Toulouse Paul Sabatier, CNRS, Toulouse INP-ENSEEIHT, Toulouse, France. E-mail: cyril.gadal@imft.fr

P. Delorme
School of Geography and Environmental Science, University of Southampton, Southampton, UK.

C. Narteau
Institut de Physique du Globe de Paris, Université de Paris, CNRS, Paris, France.

G.S.F. Wiggs
School of Geography and the Environment, University of Oxford, Oxford, UK.

M. Baddock
Geography and Environment, Loughborough University of Technology, Loughborough, UK.

J.M. Nield
School of Geography and Environmental Science, University of Southampton, Southampton, UK.

P. Claudin
Physique et Mécanique des Milieux Hétérogènes, CNRS, ESPCI Paris, PSL Research University, Université de Paris, Sorbonne Université, Paris, France. E-mail: philippe.claudin@espci.fr

orientation of the giant dunes. We quantify these similarities and differences and provide a physical understanding of the relevant aerodynamical regimes to relate them to the daily cycle of the turbulent atmospheric boundary layer over a dune pattern of given wavelength. We conclude by identifying the conditions under which the ERA5-Land reanalysis data can or can't be used to study dune morphodynamics. We also propose that, in multidirectional wind regimes, deflections of specific winds could explain the occurrence of secondary dune patterns with a different orientation than the primary structures between which they grow.

Keywords Atmospheric boundary layer · Sand dunes · Fluid-structure interactions

1 Introduction

The description of turbulent flows over a complex topography is a rich and active subject, that is relevant for a large variety of different environmental systems (Finnigan et al. 2020). For example, the flow over hills is of primary interest for wind power, meteorological and air pollution phenomena (Taylor et al. 1987). The properties of these flows are also key to the understanding of the formation of ocean surface wind-driven waves (Sullivan and McWilliams 2010), dissolution bedforms (Claudin et al. 2017), or sedimentary ripples and dunes (Charru et al. 2013; Courrech du Pont 2015). Importantly, the troposphere presents a vertical structure, with a lower convective boundary layer, of typical kilometer-scale thickness, capped by a stably stratified region (Stull 1988). The largest topographic obstacles as mountains can therefore interact with this upper region, for example leading to internal wave generation or significant wind disturbances, such as downslope winds in lee sides (Durran 1990).

Looking at the wind close to the surface, two topographic feedbacks on the flow, although related, can be commented separately. There is a first effect on the wind intensity: the flow accelerates on the upwind slope and slows down on the downwind one (Baddock et al. 2011), with a speed-up factor essentially proportional to the obstacle aspect ratio here a ref?. Importantly, the velocity maximum is typically shifted upwind of the obstacle crest. This behaviour has been theoretically predicted by means of asymptotic analysis of a neutrally stratified boundary-layer flow over an obstacle of vanishing aspect ratio (Jackson and Hunt 1975; Mason and Sykes 1979; Sykes 1980; Hunt et al. 1988; Belcher and J.C.R. 1998). Experiments in flumes (Zilker et al. 1977; Zilker and Hanratty 1979; Frederick and Hanratty 1988; Poggi et al. 2007), in wind tunnel (Gong and Ibbetson 1989; Finnigan et al. 1990; Gong et al. 1996) and in field conditions (Taylor and Teunissen 1987; Claudin et al. 2013; Fernando et al. 2019; Lü et al. 2021), have also documented this effect. Interestingly, a similar behaviour exists for the pressure perturbation, but with a slight downwind shift for the pressure minimum (Claudin et al. 2021). The second effect is the flow deflection that occurs when the incident wind direction is not perpendicular to the ridge crest. While predicted to be small (less than $10°$) in the linear regime valid for shallow topography (Gadal et al. 2019), significant flow steering has been reported in the field on the downwind side of steep enough obstacles, such as mountain ranges (Kim et al. 2000; Lewis et al. 2008; Fernando et al. 2019) or well developed sand dunes (Walker et al. 2009; Hesp et al. 2015; Walker et al. 2017; Smith et al. 2017).

For practical reasons, wind measurement over sand dunes have been performed over rather small bedforms, typically a few meters high only – that is tens of meters in length. Giant dunes, with kilometer-scale wavelengths and heights of tens of meters, are more difficult to investigate although they provide, for several reasons, a choice configuration for the study of turbulent flows over a complex topography. First of all, one expects larger wind disturbances for larger obstacles. Second, their large size make them interact with the vertical structure of the atmosphere (Andreotti et al. 2009). Also, they usually form large patterns in sand seas and thus behave as rather clean periodic perturbations, in contrast with isolated hills. Finally, because the morphodynamics of aeolian bedforms are strongly dependent on the local wind regime (Livingstone and Warren 1996), one can expect to see the consequences of the wind disturbances on smaller dunes, in a similar way as what has been reported for the effect of dunes on impact ripples (Howard 1977; Hood et al. 2021).

Arid areas have been much studied at the desert scale from climate reanalyses based on global atmospheric models (Blumberg and Greeley 1996; Livingstone et al. 2010; Ashkenazy et al. 2012; Jolivet et al. 2021; Hu et al. 2021), such as ERA-40, ERA-Interim or ERA-5 (Uppala et al. 2005; Dee et al. 2011; Hersbach et al. 2020). However, the spatial resolution (tens of kilometers) of these reanalyses implies average quantities that do not resolve the smaller scales, ranging from individual dunes to the border of mountains (Livingstone et al. 2010). Lately, the release of ERA5-Land allows to push back this limitation by providing up to 70 years of hourly wind predictions at a 9 km spatial resolution (Muñoz-Sabater et al. 2021). However, its validity remains to be studied, especially in areas where data assimilation is low (such as deserts).

In this work, we compare local wind speeds and directions measured in four different places inside and north of the giant-dune field of the Namib sand sea to the regional predictions of the ERA5-Land climate reanalysis. When the meteorological stations are surrounded by a relatively flat environment, we show that local measurements and regional predictions agree well with each other. The find that the agreement is also good in the interdune areas of the sand sea, except for the weak winds blowing at night in a direction oblique to the orientation of the giant dunes (section 2). Furthermore, we are able to link the magnitude of these differences to the circadian cycle of the atmospheric boundary layer (section 3). Finally, we draw implications of the wind disturbances on smaller-scale dunes (section 4).

2 Wind regimes across the Namib Sand Sea

We have measured the wind regime in four different sites of Namibia, representative of various environments across and nearby the Namib desert (Fig. 1). The Adamax station is located near the Adamax salt pan, in a highly vegetated area. The Huab station, on the coast at the outlet of the Huab river, is in an arid place where 60-m scale barchan dunes develop. These two stations are located in a relatively flat quantify how flat is flat ? environment. In contrast, the Deep Sea and South Namib stations are located in the interdune between tens of meters high giant linear dunes with kilometer-scale wavelengths and superimposed patterns. In this section, we describe and compare winds from local measurements and climate reanalysis predictions.

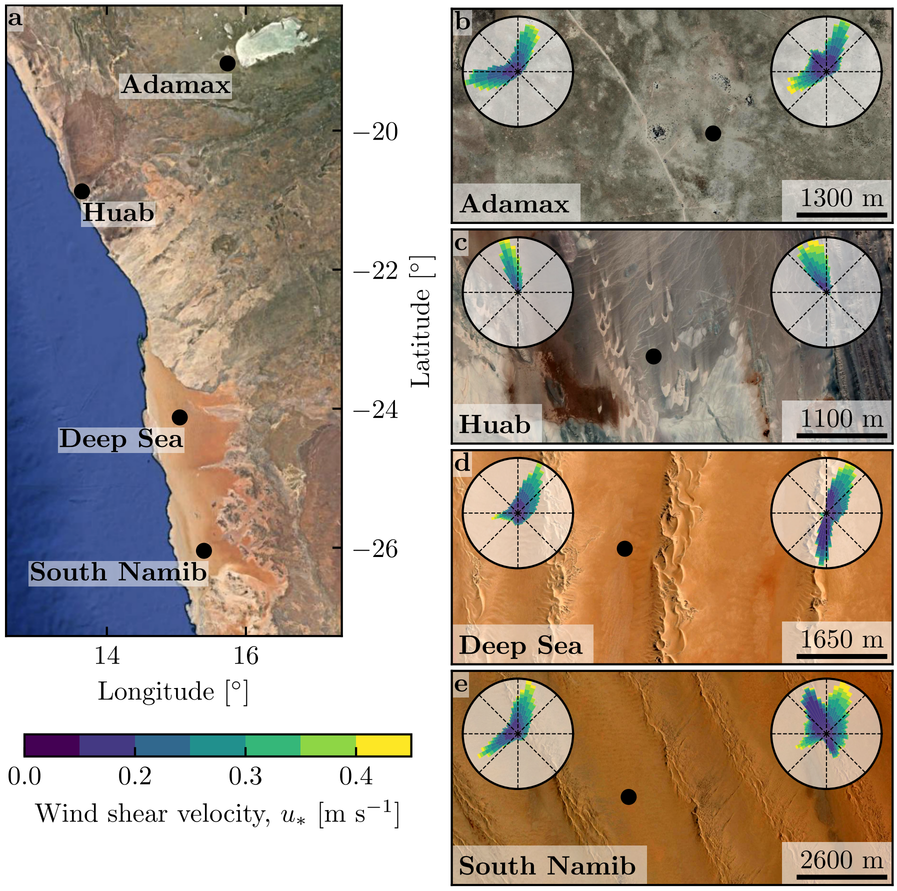

Fig. 1 Wind data used in this study **a**: Location of the different sites in Namibia. **b-e**: Satellite images of these different environements (Google-Earth, Maxar Technologies, CNES/Airbus). In each subplot, the left and right wind roses represent the data from the ERA5-Land climate reanalysis and the local wind stations, respectively. Note that the bars show the direction towards which the wind blows. The black dots show the location of local wind stations.

2.1 Wind and elevation data

Local winds are measured at meteorological stations located in these four different places (black dots in Fig. 1). The wind strength and direction are sampled every 10 minutes by cup anemometers and wind vanes, at heights between 2 m and 3 m depending on the station. The available period of measurements ranges from 1 to 5 discontinuous years distributed between 2012 and 2020 (Suppl. Fig. S1). We checked that at least one complete seasonal cycle is available at each station. Regional winds are extracted at the same locations and periods from the ERA5-Land dataset, which is a replay at a smaller spatial resolution of ERA5, the latest climate reanalysis from the ECMWWF (Hersbach et al. 2020; Muñoz-Sabater et al. 2021). It provides hourly predictions of the 10-m wind velocity and direction at a spatial resolution of $0.1^\circ \times 0.1^\circ$ ($\simeq 9$ km in Namibia).

For comparison, the local measurements are averaged into 1-hr bins centered on the temporal scale of the ERA5-Land estimates (Suppl. Fig. S2). As the wind velocities of both datasets are provided at different heights, we convert them into shear velocities (Suppl. Mat. section 1), characteristic of the turbulent wind profile, which are then used together with the wind direction for further analysis. Wind roses in Fig. 1(b–e) show the resulting wind data.

Dune properties are computed using autocorrelation on the 30-m Digital Elevation Models (DEMs) of the shuttle radar topography mission (Farr et al. 2007). For the South Namib and Deep Sea stations, we obtain respectively orientations of 85° and 125° with respect to the North, wavelengths of 2.6 km and 2.3 km and amplitudes of 45 m and 20 m (Suppl. Fig. S4 for more details).

2.2 Comparison of local and regional winds

The obtained wind regimes are shown in figure 1. In the Namib, the regional wind patterns are essentially controlled by the see breeze, resulting in strong northward components (sometimes slightly deviated by the large scale topography mountain?) present in all regional wind roses (Lancaster 1985). These daytime winds are dominant during the second-half of the year (September-January). In winter, an additional easterly component can be recorded during the night, induced by the combination of katabatic winds forming in the mountains, and infrequent 'berg' winds, which are responsible of the high wind velocities observed (Lancaster et al. 1984). The frequency of these easterly components decreases from the inland to the coast. As a result, bidirectional wind regimes within the Namib Sand Sea and at the Adamax salt pan (Fig. 1b,d,e) and a unidirectional wind regime on the coast at the outlet of the Huab River (Fig. 1c) are observed.

In the case of the Adamax and Huab stations, the time series of wind speed and direction from the regional predictions quantitatively match those corresponding to the local measurements (Fig. 2a,b) and Suppl. Fig. S5). For the Deep Sea and South Namib stations within the giant dune field, we observe that this agreement is also good, but limited to the September-January time period (Fig. 2c,d). As a matter of fact, the measured wind roses exhibit additional wind components aligned with the giant dune orientation, as evidenced on the satellite images (Fig. 1c,d).

More precisely, during the February-August period, the local and regional winds in the interdune match during daytime only, i.e when the southerly/southwesterly sea breeze dominates (Figs. 2(e,f) and 3, Suppl. Fig. S6). In the late afternoon and during the night, when the northwesterly 'berg' and katabatic winds blow, measurements and predictions differ. In this case, the angular wind distribution of the local measurements exhibits two additional modes corresponding to reversing winds aligned with the giant dune orientation (purple frame in

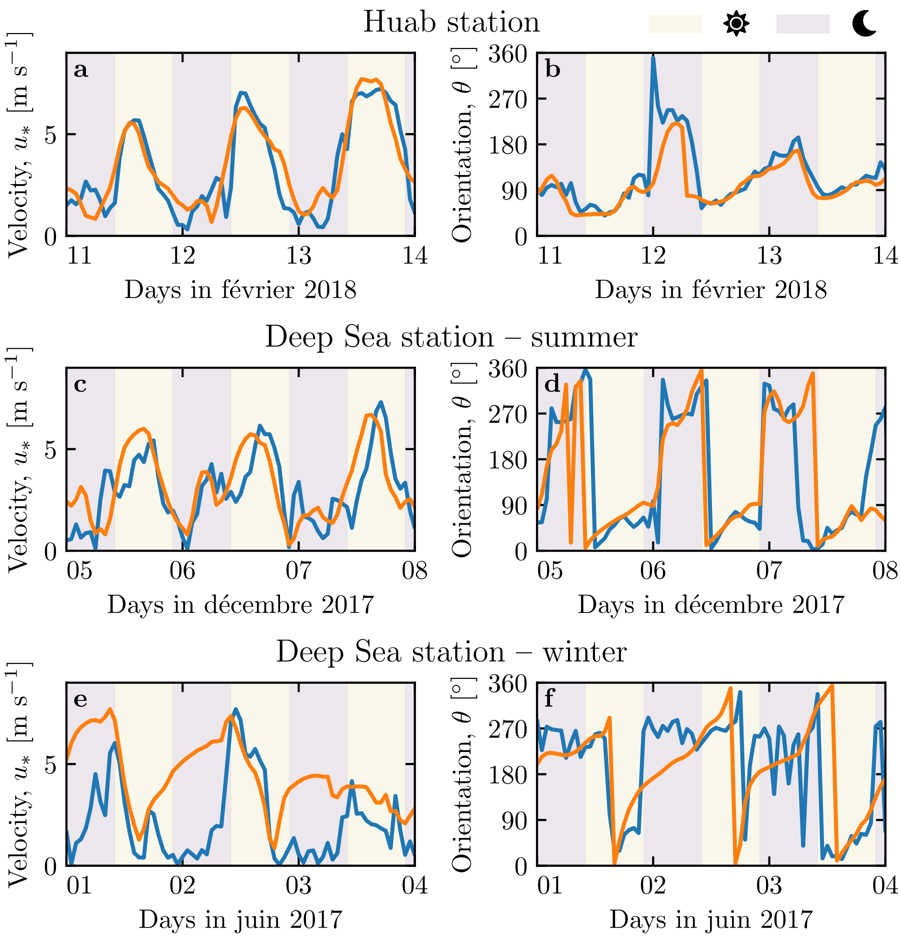

Fig. 2 Temporal comparison between the wind data coming from the ERA5-Land climate reanalysis (orange lines) and from the local measurements (blue lines). Coloured swathes indicate day (between 1000 UTC and 2200 UTC) and night (before 1000 UTC or after 2200 UTC) **a-b**: Huab station. **c-d**: Deep Sea station in winter. **e-f**: Deep Sea station in summer.

Fig. 3, Suppl. Figs. S6 and S7). This deviation is also associated with a global attenuation of the wind strength (Suppl. Fig. S8). Remarkably, all these figures show that this wind reorientation and attenuation processes typically occur at low wind velocities, typically for $u_* \lesssim 0.1$ m s^{-1}. For shear velocities larger than $\simeq 0.25$ m s^{-1}, the wind reorientation is not significant. Finally, for intermediate shear velocities, moments of reorientation along the dune crest and others with no reorientation can both be observed (Suppl. Fig. S7). CHECK the above lines cf. δu

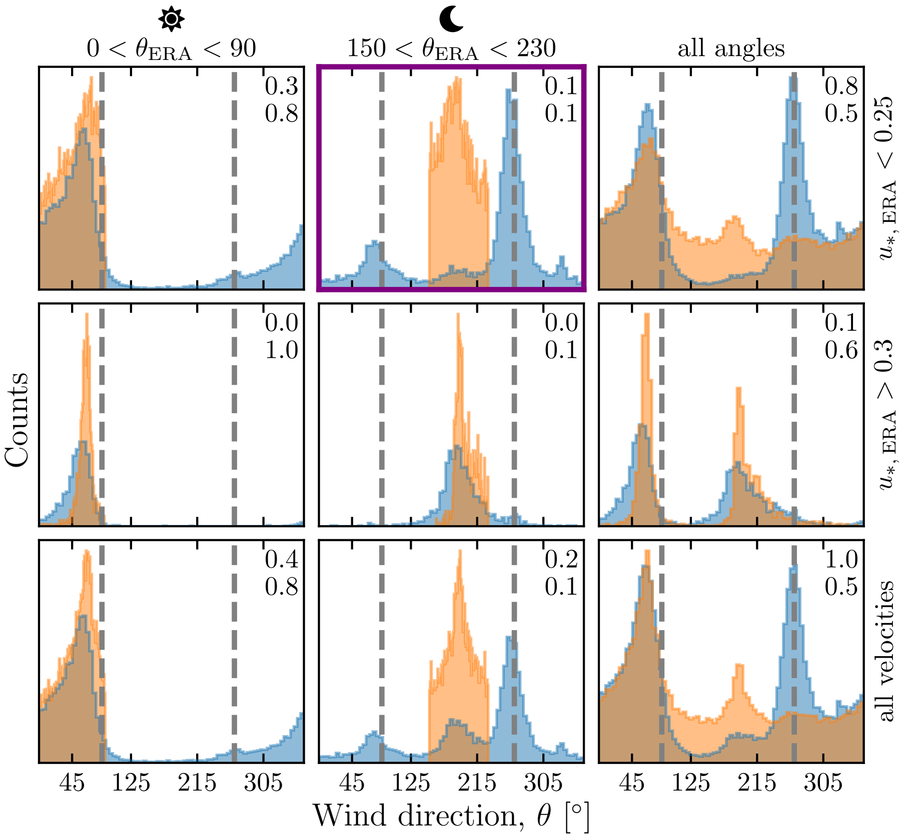

Fig. 3 Distributions of wind direction at the Deep Sea Station for the ERA5-Land climate reanalysis (orange) and the local measurements (blue). In each subplot, both distributions are plotted from the same time steps, selected with constraints on the wind direction (columns) and/or wind velocity (rows) of the ERA5-Land dataset. The gray vertical dashed lines indicate the dune orientation. The numbers at the top right give the percentage of time steps selected in each sub-range, as well as the percentage of them corresponding to the day (between 1000 UTC and 2200 UTC). The purple frame highlights the regime (small wind velocities, nocturnal summer wind) in which the data from both datasets differ. A similar figure can be obtained for the Deep Sea station (Suppl. Fig. S6).

3 Influence of wind speed and circadian cycle on the atmospheric boundary layer

The wind deflection induced by linear dunes has so far mainly been related to the angle between wind direction and crest orientation, with a maximum deflection for angles between 30° and 70° (Walker et al. 2009; Hesp et al. 2015). In the analysed data, the most deflected wind at both Deep Sean and South Namib stations is the most perpendicular to the giant dunes (Fig. ??). The incident wind direction then does not seem to be the only parameter controlling the wind deflection. In contrast, a different behaviour is observed between low and high wind velocities, suggesting a change in hydrodynamical regime. In this section, we discuss the relevant parameters associated with the dynamical mechanisms that govern the interactions between the atmospheric boundary layer flow and topographical obstacles. This analysis allows us to provide a physics-based interpretation the observations.

3.1 Flow over a modulated bed

Taking as a reference the turbulent flow over a flat bed, the general framework of this study is the understanding and the description of the flow response to a bed modulation. Without loss of generality, we can consider in this context an idealised bed elevation in the form of parallel sinusoidal ridges, with wavelength λ (or wavenumber $k = 2\pi/\lambda$) and amplitude ξ_0, and where the reference flow direction makes a given angle with respect to the ridge crest (Andreotti et al. 2012). Part of this response, on which we focus here, is the flow deflection by the ridges. In a simplified way, it can be understood from the Bernoulli principle (Hesp et al. 2015): as the flow approaches the ridge crest, the compression of the streamlines results in larger flow velocities, and thus lower pressures (Rubin and Hunter 1987). An incident flow oblique to the ridge is then deflected towards lower pressure zones, i.e towards the crest. Turbulent dissipation tends to increase this effect downstream, resulting in along the crest wind deflection in the lee side (Gadal et al. 2019).

Flow confinement below a capping surface, which enhances streamline compression, has a strong effect on the hydrodynamic response and typically increases flow deflection. This is the case for bedforms forming in open channel flows such as rivers (Fourrière et al. 2010; Unsworth et al. 2018). This is also relevant for aeolian dunes as they evolve in the turbulent atmospheric boundary layer (ABL) capped by the stratified free atmosphere (FA) (Andreotti et al. 2009). Two main mechanisms, associated with dimensionless numbers, must then be considered (Fig. 4). First, topographic obstacles typically disturb the flow over a characteristic height similar to their length. As flow confinement is characterised by a thickness H, the interaction between the dunes and the wind in the ABL is well captured by the parameter kH. The height H is directly related to the radiative fluxes at the Earth surface. It is typically on the order of a kilometre, but significantly varies with the circadian and seasonal cycles. Emerging and small dunes, with wavelengths in the range 20 to 100 m, are not affected by the confinement, corresponding to $kH \gg 1$. For giant dunes with kilometric wavelengths, however, their interaction with the FA is significant (Andreotti et al. 2009). This translates into a parameter kH in the range 0.02–5, depending on the moment of the day and the season. A second important mechanism is associated with the existence of a thin intermediate so-called capping layer between the ABL and the FA. It is characterised by a density jump $\Delta\rho$, which controls the 'rigidity' of this interface, i.e. how much its deformation affects streamline compression. This is usually quantified using the Froude number (Vosper 2004; Stull 2006; Sheridan and Vosper 2006; Hunt

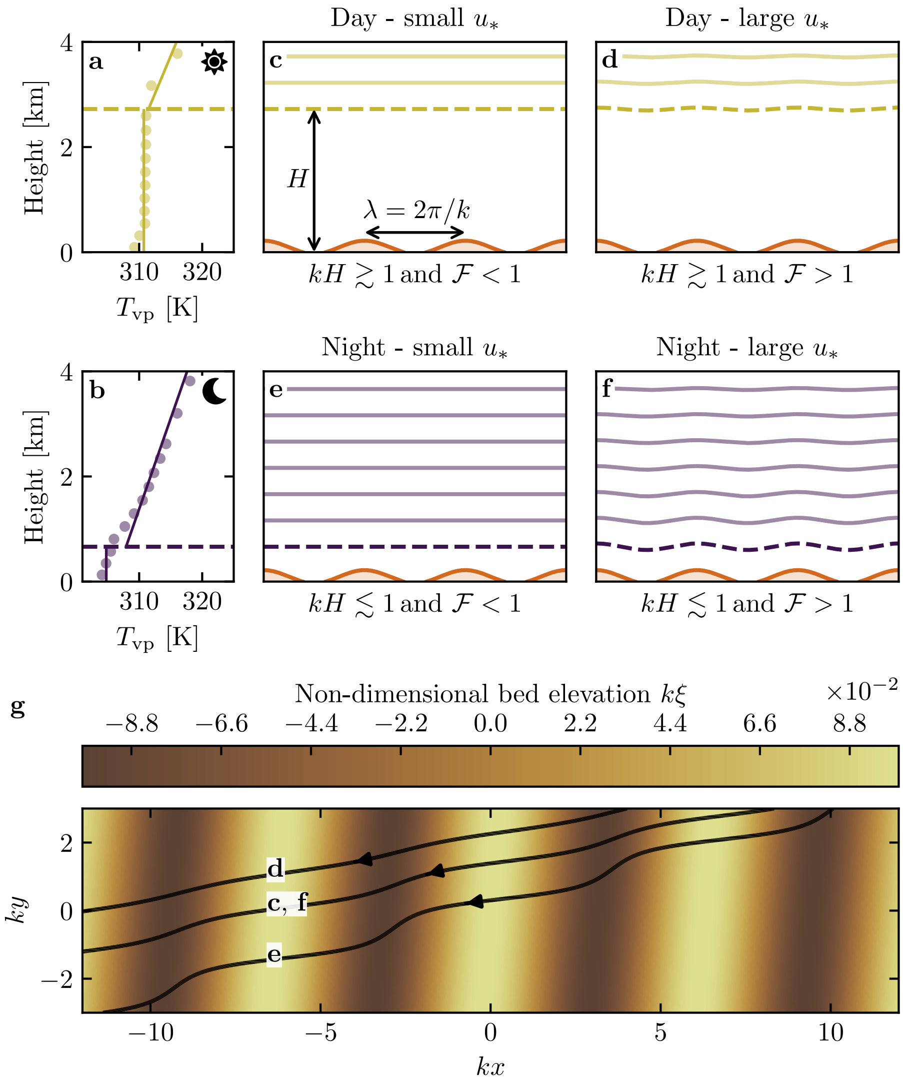

Fig. 4 **a-b**: Vertical profiles of the virtual potential temperature at 2 different time steps (day - 03/11/2015 - 1200 UTC, night - 01/13/2013 - 0900 UTC) at the Deep Sea station. Dots: data from the ERA5 reanalysis. Dashed lines: boundary layer height given by the ERA5 reanalysis (Suppl. Mat. section 2). Plain lines: vertical (boundary layer) and linear (free atmosphere) fits to estimate the stratification properties. **c-f**: Sketches representing the interaction between the giant dunes and the atmospheric flow for different meteorological conditions. **g**: Streamlines over a sinusoidal topography $\xi(x, y)$ qualitatively representing the effect of low, medium and strong flow confinement, in relation to the above panels (see Appendix 1 for more details). add arrow with reference wind

et al. 2006; Jiang 2014):

$$\mathcal{F} = \frac{U}{\sqrt{\dfrac{\Delta\rho}{\rho_0} g H}}, \tag{1}$$

where U is the wind velocity at the top of the ABL and ρ_0 its average density. The intensity of the stratification, i.e. the amplitude of the gradient $|\partial_z \rho|$, also impact ability to deform the capping layer under the presence of an underlying obstacle, and thus affects the influence of flow confinement. This can be quantified using the internal Froude number (Vosper 2004; Stull 2006; Sheridan and Vosper 2006; Hunt et al. 2006; Jiang 2014) $\mathcal{F}_\mathrm{I} = kU/N$, where $N = \sqrt{-g\partial_z\rho/\rho_0}$ is the the Brunt-Väisälä frequency (Stull 1988). Both Froude numbers have in practice the same qualitative effect on flow confinement, and we shall restrict the main discussion to $\mathcal{F}$ only.

This theoretical framework in mind, the smallest wind disturbances are expected to occur during the day, when the ABL depth is the largest and comparable to the dune wavelength ($kH \gtrsim 1$), which correspond to a weak confinement situation (Fig. 4c,d). On the contrary, large wind disturbances are expected to occur during the night, when the confinement is mainly induced by a shallow ABL (Fig. 4e). However, this strong confinement can be somewhat reduced in the case of strong winds, corresponding to large values of the Froude number (Fig. 4f). This is qualitative agreement with the transition from deflected to non-deflected winds related to low and high velocities observed in the data (Sec. 2.2).

3.2 Flow regime diagrams

We can go one step further and analyse how our data quantitatively spread over the different regimes discussed above. For that purpose, one needs to compute kH and $\mathcal{F}$ from the time series. H, U and the other atmospheric parameters can be deduced from the various vertical profiles (temperature, humidity) available in the ERA5 climate reanalysis (Suppl. Mat. section 2). We quantify the flow deflection δ_θ as the minimal angle between the wind orientations comparing the local measurements and the regional predictions. We also compute the relative velocity modulation as

$$\delta_\mathrm{u} = \frac{u_*^\mathrm{ERA} - u_*^\mathrm{station}}{u_*^\mathrm{ERA}}. \tag{2}$$

These two quantities are represented as maps in the plane ($\mathcal{F}$, kH) (Fig. 5a,b), and one can clearly identify different regions in these graphs. Small wind disturbances (small δ_θ and δ_u) are located in the top-right part of the diagrams, corresponding to a regime with low-interaction as well as low-confinement (kH and $\mathcal{F}$ large enough, Fig. 4d). Lower values of kH (stronger interaction) or of Froude number (stronger confinement) both lead to an increase in wind disturbances, both in terms of orientation and velocity. Below a crossover value

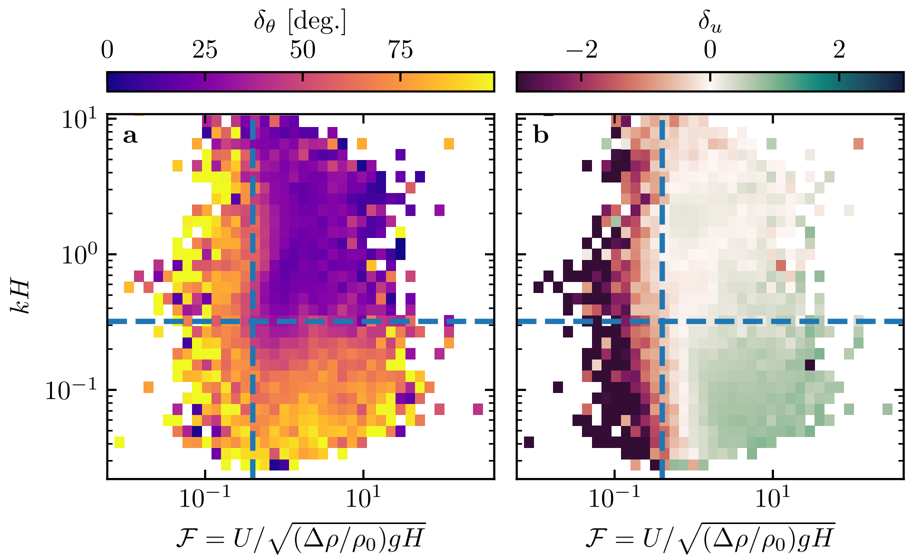

Fig. 5 Regime diagrams of the wind deviation δ_θ (**a**) and relative attenuation/amplification δ_u (**b**) in the space ($\mathcal{F}$, kH), containing the data from both the Deep Sea and South Namib stations. Blue dashed lines empirically delimit the different regimes. The point density in each bin of the diagrams is shown in Suppl. Fig. S11. Similar regime diagrams in the spaces ($\mathcal{F}_\mathrm{I}$, kH) and ($\mathcal{F}_\mathrm{I}$, $\mathcal{F}$) are shown in Suppl. Fig. S12. ticks on x-axis ?

$kH \simeq 0.3$, wind disturbance is less sensitive to the $\mathcal{F}$-value, probably due to enhanced non-linear effects linked to strong flow modulation by the obstacle when confinement is strong more precise arguments?. The Froude number also controls a transition from damped to amplified wind velocities in the inter-dune, with a crossover around $\mathcal{F} \simeq 0.4$ (Fig. 5b). Such an amplification is rather unexpected. Checking the occurrence of the corresponding data, it appears that they are mainly associated with the wind coming from the South, when it blows at the end of day, but in summer time only although it is also present in winter an additional suppl. fig. ?. This effect may be linked to a change in the flow behaviour in the lee side of the obstacle (lee waves, hydraulic jumps, rotors) but further measurements are clearly needed in order to assess the different possibilities (Baines 1995; Vosper 2004).

4 Discussion

The comparison of local (direct measurements) and regional (climate reanalysis) wind data reveals the giant dune feedback on the wind flow. In flat areas, the agreement between the two confirms the ability of the ERA5-Land climate reanalysis to predict the wind regime down to scales ~ 10 km, i.e the model grid. When smaller scale topographies are present (giant dunes in our case), locally measured winds can significantly differ from the regionally predicted ones. This is the case when the disturbances induced by the dunes

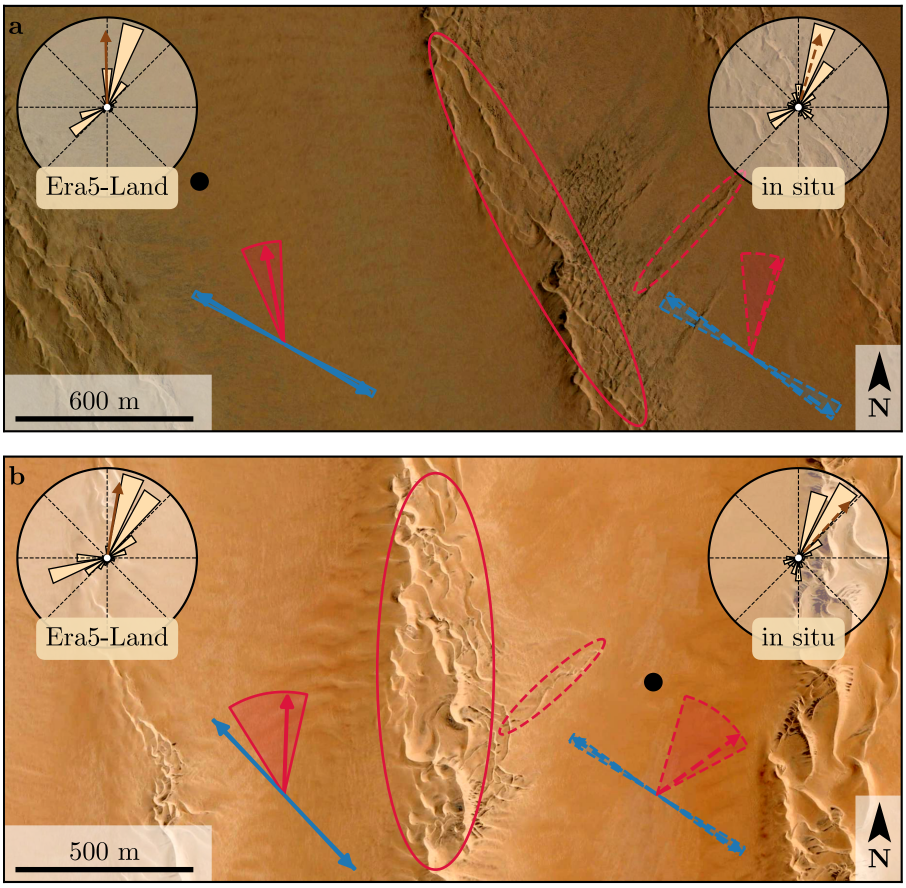

Fig. 6 Implications for smaller scale patterns in (**a**) the South Namib and (**b**) Deep Sea. The ellipses indicate the different types of elongating dunes, at large (plain line) and small (dashed line) scales. Dune orientation are predicted using the model of Courrech du Pont et al. (2014) from the sand flux angular distributions, shown here (roses and resultant transport direction) for typical values (grain size 180 μm, flux-up ratio of 1.6). Code for corresponding arrows: use of ERA5-Land data (plain line), use of local measurements (dashed line), prediction for the bed instability growth mechanism (blue), prediction for the elongation growth mechanism (red). Wedges show the uncertainty on the orientation calculation when parameters are varied. The black dots indicate the location of the meteorological stations with respect to the dunes. See Appendix 2 for additional details.

interact with the lower part of the ABL vertical structure, which presents circadian variations. During the day, when the capping layer is typically high, this interaction is small, and the ERA5-Land predictions are also quantitatively consistent with the local data. During the night, however, the presence of a shallow atmospheric boundary layer induces a strong confinement of the flow, and is associated with large wind deflection by the dunes. Importantly, we find that this effect can be counterbalanced for large wind velocities, which are capable of deforming the capping layer, thus decreasing the influence of the confinement.

The theoretical computation of the wind disturbances induced by sinusoidal ridges under flow confinement has been performed in the linear limit (Andreotti et al. 2009, 2012), i.e. when the aspect ration of these ridges is small ($k\xi_0 \ll 1$). These models are able to qualitatively reproduce the observed wind deflection (Appendix 1, Suppl. Figs. S12 and S13), and thus provide the physical support for the hydrodynamic picture we propose here. They however cannot reach the magnitude of these observations, probably due to the presence of expected non-linearities in high confinement situations linked to strong flow modulations. Besides, these linear calculations only predict wind attenuation in the interdune, in contrast with the observed enhanced velocities associated with particular summer evening winds from the South. Some other models also predict different spatial flow structures such as lee waves and rotors (Baines 1995; Vosper 2004), which of course cannot be observed by our single point measurements. Data at different places along and across the ridges are needed to investigate and possibly map such flow structures, and for further comparisons with the models.

This study highlights the interaction between giant dunes and the atmospheric boundary layer. It then supports the debated idea that the capping layer acts as a bounding surface impacting the dune dynamics, and limiting dune growth in particular (Andreotti et al. 2009), as opposed to an unconstrained growth ever-slower with size (Eastwood et al. 2011; Gunn et al. 2021). Interestingly, this mechanism would allow for the inference of the ABL depth from the giant bedforms spacing where measurements are not feasible or available, as e.g. performed by Lorenz et al. (2010) on Titan.

This interaction also has important implications for smaller scales bedforms, as illustrated in Fig. 6. In the Namib Sand Sea, small linear dunes (~ 50 m -wide) are present in the interdune between giant linear dunes (~ 2 km -wide). Strangely enough, the small dunes do not have the same orientation as the large ones, and sometimes denotes as 'crossing dunes'. While differences between large and small scale dune patterns are observed ubiquitously, they are now largely attributed to the presence of two different dune growth mechanisms, leading to two different dune patterns (orientations and/or morphologies) for the same wind regime (Courrech du Pont et al. 2014; Runyon et al. 2017; Lü et al. 2017; Song et al. 2019; Gadal et al. 2020; Hu et al. 2021). Here, however, we can get the orientations of the small and giant linear dunes from the same dune growth mechanism (elongating mode), respectively using the locally measured and regionally predicted winds (red arrows in Fig. 6). The feedback of the giant dunes on the wind described in this study then provides an explanation for the existence of these small linear dunes elongating across the interdune, as yet unresolved. Further studies are of course needed to confirm this hypothesis. These crossing dunes could provide additional constraints for the inference of local winds from bedforms, similarly to what is currently performed on Mars using ripple orientations (Liu and Zimbelman 2015; Hood et al. 2021).

Acknowledgements We would like to acknowledge the contributors of the following open-source python librairies, Matplotlib (Hunter 2007), Numpy (Harris et al. 2020) and Scipy (Virtanen et al. 2020), which provide an incredibly efficient ecosystem allowing scientific research in Python.

ERA5 and ERA5-Land datasets are publicly available at the Copernicus Climate Change Service (C3S) Climate Data Store. The locally measured wind data can be found at upload on public data repository. The digital elevation models from the Shuttle Radar Topography Mission are publicly available from Nasa servers, and can be downloaded at https://dwtkns.com/srtm30m/. Fully documented codes used to analyse this study are available at https://github.com/Cgadal/GiantDunes (will be made public upon acceptance of this manuscript for publication).

[citing all grants ...] TOAD

Appendix 1: Linear theory of wind response to topographic perturbation

Following the work of Fourrière et al. (2010), Andreotti et al. (2012) and Andreotti et al. (2009), we briefly expose in this appendix the framework of the linear response of a turbulent flow to a topographic perturbation of small aspect ratio. As a general bed elevation can be decomposed into Fourier modes, we focus here on a sinusoidal topography:

$$\xi = \xi_0 \cos\left[k\left(\cos(\alpha)x + \sin(\alpha)y\right)\right], \tag{3}$$

which is also a good approximation for the giant dunes observed in the Deep Sea and South Namib Station (Fig. 1 and Suppl. Fig. S4). x and y are the streamwise and spanwise coordinates, $k = 2\pi/\lambda$ the wavenumber of the sinusoidal perturbation, and α its crest orientation with respect to the y-direction. The two components of the basal shear stress $\boldsymbol{\tau} = \rho_0 u_* \boldsymbol{u}_*$, constant in the flat bottom reference case, can then be generically written as:

$$\tau_x = \tau_0 \left(1 + k\xi_0 \sqrt{\mathcal{A}_x^2 + \mathcal{B}_x^2} \cos\left[k\left(\cos(\alpha)x + \sin(\alpha)y\right) + \phi_x\right]\right), \tag{4}$$

$$\tau_y = \tau_0\, k\xi_0 \sqrt{\mathcal{A}_y^2 + \mathcal{B}_y^2} \cos\left[k\left(\cos(\alpha)x + \sin(\alpha)y\right) + \phi_y\right], \tag{5}$$

where τ_0 is the reference basal shear stress on a flat bed. We have defined the phase $\phi_{x,y} = \tan^{-1}\left(\mathcal{B}_{x,y}/\mathcal{A}_{x,y}\right)$ from the in-phase and in-quadrature hydrodynamical coefficients $\mathcal{A}_{x,y}$ and $\mathcal{B}_{x,y}$. They are functions of k and of the flow conditions, i.e the bottom roughness, the vertical flow structure and the incident flow direction, and the theoretical framework developed in the above cited papers proposes methods to compute them in the linear regime.

Following Andreotti et al. (2012), the effect of the incident wind direction can be approximated by the following expressions:

$$\mathcal{A}_x = \mathcal{A}_0 \cos^2\alpha, \tag{6}$$

$$\mathcal{B}_x = \mathcal{B}_0 \cos^2\alpha, \tag{7}$$

$$\mathcal{A}_y = \frac{1}{2}\mathcal{A}_0 \cos\alpha \sin\alpha, \tag{8}$$

$$\mathcal{B}_y = \frac{1}{2}\mathcal{B}_0 \cos\alpha \sin\alpha, \tag{9}$$

where $\mathcal{A}_0$ and $\mathcal{B}_0$ are now two coefficients independent of the dune orientation α, corresponding to the transverse case ($\alpha = 0$). For a fully turbulent boundary layer capped by a stratified atmosphere, these coefficients depend on kH, kz_0, $\mathcal{F}$ and $\mathcal{F}_\mathrm{I}$ (Andreotti et al. 2009). In this study, we assume a constant hydrodynamic roughness $z_0 \simeq 1$ mm (Suppl. Mat. section 1). For the considered giant dunes, this leads to $kz_0 \simeq 2 \cdot 10^{-6}$, as their wavelength is $\lambda \simeq 2.4$ km (or $k \simeq 2 \cdot 10^{-3}$ m^{-1}). Values of z_0 extracted from field data indeed typically fall between 0.1 mm and 10 mm (Sherman and Farrell 2008; Field and Pelletier 2018). Importantly, $\mathcal{A}_0$ and $\mathcal{B}_0$ do not vary much in the corresponding range of kz_0 (Fourrière et al. 2010), and the results presented here are robust with respect to this choice.

With capping a layer height and Froude numbers computed from the ERA5-Land time series, the corresponding $\mathcal{A}_0$ and $\mathcal{B}_0$ can be deduced, allowing to produce maps as displayed in Suppl. Fig. S13. Interestingly, it shows similar regimes as in the diagrams of Fig. 5 and Fig. S12a,b, supporting the physics picture. However, the matching remains qualitative only. As a matter of fact, the linearity assumption of the theoretical framework requires $(|\tau| - \tau_0)/\tau_0 \ll 1$, which translates into $k\xi\sqrt{\mathcal{A}_0^2 + \mathcal{B}_0^2} \ll 1$. In our case, the giant dune morphology gives $k\xi_0 \simeq 0.1$, which means that one quits the regime of validity of the linear theory when the coefficient modulus $\sqrt{\mathcal{A}_0^2 + \mathcal{B}_0^2}$ becomes larger than a few units. In accordance with the theoretical expectations, these coefficients present values on the order of unity ($\mathcal{A}_0 \simeq 3$ and $\mathcal{B}_0 \simeq 1$) in unconfined situations (Claudin et al. 2013; Lü et al. 2021). In contrast and as illustrated in Suppl. Fig. S12a,b, larger values are predicted in case of strong confinement, which does not allow us to proceed to further quantitative comparison with the data.

Finally, the linear model is also able to reproduce the enhancement of the flow deflection over the sinusoidal ridges when $\sqrt{\mathcal{A}_0^2 + \mathcal{B}_0^2}$ is increased (Suppl. Fig. S13). Here, using $k\xi_0 \simeq 0.1$ to be representative of the amplitude of the giant dunes at the Deep Sea station, the coefficient modulus is bounded to 10.

Appendix 2: Sediment transport and dune morphodynamics

We summarise in this appendix the sediment transport and dune morphodynamics theoretical framework leading to the prediction of sand fluxes and dune orientations from wind data.

Sediment transport — The prediction of sand fluxes from wind data has been a long standing issue in aeolian geomorphological studies (Fryberger and Dean 1979; Pearce and Walker 2005; Sherman and Li 2012; Shen et al. 2019). Based on laboratory studies in wind tunnels (Rasmussen et al. 1996; Iversen and Rasmussen 1999; Creyssels et al. 2009; Ho et al. 2011), as well as physical considerations (Ungar and Haff 1987; Andreotti 2004; Durán et al. 2011; Pähtz and Durán 2020), it has been shown that the steady saturated saltation flux over a flat sand bed depends linearly on the shear stress:

$$\frac{q_{\mathrm{sat}}}{Q} = \varOmega\sqrt{\varTheta_{\mathrm{th}}}\left(\varTheta - \varTheta_{\mathrm{th}}\right), \tag{10}$$

where $\varOmega$ is a proportionality constant, $Q = d\sqrt{(\rho_{\mathrm{s}} - \rho_0)gd/\rho_0}$ is a characteristic flux, $\varTheta = \rho_0 u_*^2/(\rho_{\mathrm{s}} - \rho_0)gd$ the Shields number, and $\varTheta_{\mathrm{th}}$ its threshold value below which saltation vanishes. $\rho_{\mathrm{s}} = 2.6$ g cm^{-3} and $d = 180$ μm are the grain density and diameter, and g is the gravitational acceleration. The shear velocity, and consequently the Shields number as well as the sediment flux, are time dependent.

Recently, Pähtz and Durán (2020) suggested an additional quadratic term in Shields to account for grain-grain interactions within the transport layer at strong wind velocities:

$$\frac{q_{\mathrm{sat,\,t}}}{Q} = \frac{2\sqrt{\varTheta_{\mathrm{th}}}}{\kappa\mu}\left(\varTheta - \varTheta_{\mathrm{th}}\right)\left(1 + \frac{C_{\mathrm{M}}}{\mu}\left[\varTheta - \varTheta_{\mathrm{th}}\right]\right), \tag{11}$$

where $\kappa = 0.4$ is the von Kármán constant, $C_{\mathrm{M}} \simeq 1.7$ a constant and $\mu \simeq 0.6$ is a friction coefficient, taken to be the avalanche slope of the granular material. The fit of this law to the experimental data of Creyssels et al. (2009) and Ho et al. (2011) gives $\varTheta_{\mathrm{th}} = 0.0035$. The fit of Eq. 10 on these same data similarly gives $\varOmega \simeq 8$ and $\varTheta_{\mathrm{th}} = 0.005$. The sand flux angular distributions and the dune orientations in Fig. 6 are calculated using this law (11). We have checked that using the ordinary linear relationship (10) instead does not change the predicted dune orientations by more than a few degrees.

Dune orientations — Dune orientations are predicted with the dimensional model of Courrech du Pont et al. (2014), from the sand flux time series computed with the above transport law. Two orientations are possible depending on the mechanism dominating the dune growth: elongation or bed instability. The orientation α corresponding the bed instability is then the one that maximises the following growth rate (Rubin and Hunter 1987):

$$\sigma \propto \frac{1}{H_d W_d T}\int_0^T q_{\mathrm{crest}}|\sin\left(\theta - \alpha\right)|\,\mathrm{d}t, \tag{12}$$

where θ is the wind orientation measured with respect to the same reference as α, and H_d and W_d are dimensional constants respectively representing the dune height and width. The integral runs over a time T, which must be representative of the characteristic period of the wind regime. The flux at the crest is expressed as:

$$q_{\mathrm{crest}} = q_{\mathrm{sat}}\left[1 + \gamma|\sin\left(\theta - \alpha\right)|\right], \tag{13}$$

where the flux-up ratio γ has been calibrated to 1.6 using field studies, underwater laboratory experiments and numerical simulations. Predictions of the linear analysis of Gadal et al. (2019) give similar results.

Similarly, the dune orientation corresponding to the elongation mechanism is the one that verifies:

$$\tan(\alpha) = \frac{\langle q_{\mathrm{crest}}(\alpha)\boldsymbol{e}_{\theta}\rangle \cdot \boldsymbol{e}_{WE}}{\langle q_{\mathrm{crest}}(\alpha)\boldsymbol{e}_{\theta}\rangle \cdot \boldsymbol{e}_{SN}}, \tag{14}$$

where $\langle . \rangle$ denotes a vectorial time average. The unitary vectors $\boldsymbol{e}_{WE}$, $\boldsymbol{e}_{SN}$ and $\boldsymbol{e}_{\theta}$ are in the West-East, South-North and wind directions, respectively.

The resulting computed dune orientations, blue and red arrows in Fig. 6, then depend on a certain number of parameters (grain properties, flux-up ratio, etc.), for which we take typical values for aeolian sandy deserts. Due to the lack of measurements in the studied places, some uncertainties can be expected. We therefore run a sensibility test by calculating the dune orientations for grain diameters ranging from 100 μm to 400 μm and for a speed-up ratio between 0.1 and 10 (wedges in Fig. 6).

References

Andreotti B (2004) A two-species model of aeolian sand transport. J Fluid Mech 510:47–70

Andreotti B, Fourrière A, Ould-Kaddour F, Murray B, Claudin P (2009) Giant aeolian dune size determined by the average depth of the atmospheric boundary layer. Nature 457:1120–1123

Andreotti B, Claudin P, Devauchelle O, Durán O, Fourrière A (2012) Bedforms in a turbulent stream: ripples, chevrons and antidunes. J Fluid Mech 690:94–128

Ashkenazy Y, Yizhaq H, Tsoar H (2012) Sand dune mobility under climate change in the kalahari and australian deserts. Climatic Change 112:901–923

Baddock M, Wiggs G, Livingstone I (2011) A field study of mean and turbulent flow characteristics upwind, over and downwind of barchan dunes. Earth Surf Process Landforms 36:1435–1448

Baines PG (1995) Topographic effects in stratified flows. Cambridge university press

Belcher S, JCR H (1998) Turbulent flow over hills and waves. Annu Rev Fluid Mech 30:507–538

Blumberg DG, Greeley R (1996) A comparison of general circulation model predictions to sand drift and dune orientations. J Clim 9:3248–3259

Charru F, Andreotti B, Claudin P (2013) Sand ripples and dunes. Annu Rev Fluid Mech 45:469–493

Claudin P, Wiggs G, Andreotti B (2013) Field evidence for the upwind velocity shift at the crest of low dunes. Boundary-layer Meteorol 148:195–206

Claudin P, Durán O, Andreotti B (2017) Dissolution instability and roughening transition. J Fluid Mech 832:R2

Claudin P, Louge M, Andreotti B (2021) Basal pressure variations induced by a turbulent flow over a wavy surface. Front Phys 9:682,564

Courrech du Pont S (2015) Dune morphodynamics. C R Physique 16:118–138

Courrech du Pont S, Narteau C, Gao X (2014) Two modes for dune orientation. Geology 42:743–746

Creyssels M, Dupont P, El Moctar AO, Valance A, Cantat I, Jenkins JT, Pasini JM, Rasmussen KR (2009) Saltating particles in a turbulent boundary layer: experiment and theory. J Fluid Mech 625:47–74

Dee DP, Uppala SM, Simmons AJ, Berrisford P, Poli P, Kobayashi S, Andrae U, Balmaseda M, Balsamo G, Bauer dP, et al. (2011) The era-interim reanalysis: Configuration and performance of the data assimilation system. Q J R Meteorol Soc 137:553–597

Durán O, Claudin P, Andreotti B (2011) On aeolian transport: Grain-scale interactions, dynamical mechanisms and scaling laws. Aeolian Res 3:243–270

Durran DR (1990) Mountain waves and downslope winds. In: Atmospheric processes over complex terrain, Springer, pp 59–81

Eastwood E, Nield J, Baas A, Kocurek G (2011) Modelling controls on aeolian dune-field pattern evolution. Sedimentology 58:1391–1406

Farr TG, Rosen PA, Caro E, Crippen R, Duren R, Hensley S, Kobrick M, Paller M, Rodriguez E, Roth L, et al. (2007) The shuttle radar topography mission. Rev Geophys 45

Fernando H, Mann J, Palma J, Lundquist JK, Barthelmie RJ, Belo-Pereira M, Brown W, Chow F, Gerz T, Hocut C, et al. (2019) The perdigão: Peering into microscale details of mountain winds. Bull Amer Meteor Soc 100:799–819

Field JP, Pelletier JD (2018) Controls on the aerodynamic roughness length and the grain-size dependence of aeolian sediment transport. Earth Surf Process Landforms 43:2616–2626

Finnigan J, Raupach M, Bradley E, Aldis G (1990) A wind tunnel study of turbulent flow over a two-dimensional ridge. Boundary-layer Meteorol 50:277–317

Finnigan J, Ayotte K, Harman I, Katul G, Oldroy H, Patton E, Poggi D, Ross A, Taylor P (2020) Boundary-layer flow over complex topography. Boundary-layer Meteorol 177:247–313

Fourrière A, Claudin P, Andreotti B (2010) Bedforms in a turbulent stream: formation of ripples by primary linear instability and of dunes by nonlinear pattern coarsening. J Fluid Mech 649:287–328

Frederick KA, Hanratty TJ (1988) Velocity measurements for a turbulent non-separated flow over solid waves. Exp Fluids 6:477–486

Fryberger SG, Dean G (1979) Dune forms and wind regime. A study of global sand seas 1052:137–169

Gadal C, Narteau C, Courrech Du Pont S, Rozier O, Claudin P (2019) Incipient bedforms in a bidirectional wind regime. J Fluid Mech 862:490–516

Gadal C, Narteau C, Courrech du Pont S, Rozier O, Claudin P (2020) Periodicity in fields of elongating dunes. Geology 48:343–347

Gong W, Ibbetson A (1989) A wind tunnel study of turbulent flow over model hills. Boundary-layer Meteorol 49:113–148

Gong W, Taylor P, Dörnbrack A (1996) Turbulent boundary-layer flow over fixed aerodynamically rough two-dimensional sinusoidal waves. J Fluid Mech 312:1–37

Gunn A, Wanker M, Lancaster N, Edmonds D, Ewing R, Jerolmack D (2021) Circadian rhythm of dune-field activity. Geophys Res Lett 48:e2020GL090,924

Harris CR, Millman KJ, van der Walt SJ, Gommers R, Virtanen P, Cournapeau D, Wieser E, Taylor J, Berg S, Smith NJ, et al. (2020) Array programming with numpy. Nature 585:357–362

Hersbach H, Bell B, Berrisford P, Hirahara S, Horányi A, Muñoz-Sabater J, Nicolas J, Peubey C, Radu R, Schepers D, et al. (2020) The era5 global reanalysis. Q J R Meteorol Soc 146:1999–2049

Hesp PA, Smyth TAG, Nielsen P, Walker IJ, Bauer BO, Davidson-Arnott R (2015) Flow deflection over a foredune. Geomorphology 230:64–74

Ho TD, Valance A, Dupont P, Ould El Moctar A, Tuan Duc H, Valance A, Dupont P, Ould El Moctar A (2011) Scaling laws in aeolian sand transport. Phys Rev Lett 106:4–7

Hood DR, Ewing RC, Roback KP, Runyon K, Avouac JP, McEnroe M (2021) Inferring airflow across martian dunes from ripple patterns and dynamics. Front Earth Sci 9:702,828

Howard AD (1977) Effect of slope on the threshold of motion and its application to orientation of wind ripples. Geol Soc Am Bull 88:853–856

Hu Z, Gao X, Lei J, Zhou N (2021) Geomorphology of aeolian dunes in the western sahara desert. Geomorphology 392:107,916

Hunt J, Leibovich S, Richards K (1988) Turbulent shear flows over low hills. Q J R Meteorol Soc 114:1435–1470

Hunt JCR, Vilenski GG, Johnson ER (2006) Stratified separated flow around a mountain with an inversion layer below the mountain top. J Fluid Mech 556:105–119

Hunter JD (2007) Matplotlib: A 2d graphics environment. Computing in science & engineering 9:90–95

Iversen JD, Rasmussen KR (1999) The effect of wind speed and bed slope on sand transport. Sedimentology 46:723–731

Jackson PS, Hunt JCR (1975) Turbulent wind flow over a low hill. Q J R Meteorol Soc 101:929–955

Jiang Q (2014) Applicability of reduced-gravity shallow-water theory to atmospheric flow over topography. J Atmos Sci 71:1460–1479

Jolivet M, Braucher R, Dovchintseren D, Hocquet S, Schmitt J, ASTER Team (2021) Erosion around a large-scale topographic high in a semi-arid sedimentary basin: Interactions between fluvial erosion, aeolian erosion and aeolian transport. Geomorphology 386:107,747

Kim HG, Patel VC, Lee CM (2000) Numerical simulation of wind flow over hilly terrain. Journal of wind engineering and industrial aerodynamics 87:45–60

Lancaster J, Lancaster N, Seely M (1984) Climate of the central namib desert. Madoqua 1984:5–61

Lancaster N (1985) Winds and sand movements in the namib sand sea. Earth Surf Process Landforms 10:607–619

Lewis HW, Mobbs SD, Lehning M (2008) Observations of cross-ridge flows across steep terrain. Q J R Meteorol Soc 134:801–816

Liu ZYC, Zimbelman JR (2015) Recent near-surface wind directions inferred from mapping sand ripples on martian dunes. Icarus 261:169–181

Livingstone I, Warren A (1996) Aeolian geomorphology: an introduction. Addison Wesley Longman Ltd

Livingstone I, Bristow C, Bryant RG, Bullard J, White K, Wiggs GFS, Baas ACW, Bateman MD, Thomas DSG (2010) The namib sand sea digital database of aeolian dunes and key forcing variables. Aeolian Res 2:93–104

Lorenz R, Claudin P, Andreotti B, Radebaugh J, Tokano T (2010) A 3 km atmospheric boundary layer on titan indicated by dune spacing and huygens data. Icarus 205:719–721

Lü P, Narteau C, Dong Z, Rozier O, Du Pont SC (2017) Unravelling raked linear dunes to explain the coexistence of bedforms in complex dunefields. Nature comm 8:1–9

Lü P, Narteau C, Dong Z, Claudin P, Rodriguez S, An Z, Fernandez-Cascales L, Gadal C, Courrech du Pont S (2021) Direct validation of dune instability theory. Proc Natl Acad Sci USA 118

Mason P, Sykes R (1979) Flow over an isolated hill of moderate slope. Q J R Meteorol Soc 105:383–395

Muñoz-Sabater J, Dutra E, Agustí-Panareda A, Albergel C, Arduini G, Balsamo G, Boussetta S, Choulga M, Harrigan S, Hersbach H, et al. (2021) Era5-land: A state-of-the-art global reanalysis dataset for land applications. Earth Syst Sci Data 13:4349–4383

Pähtz T, Durán O (2020) Unification of aeolian and fluvial sediment transport rate from granular physics. Phys Rev Lett 124:168,001

Pearce KI, Walker IJ (2005) Frequency and magnitude biases in the 'Fryberger' model, with implications for characterizing geomorphically effective winds. Geomorphology 68:39–55

Pelletier JD, Field JP (2016) Predicting the roughness length of turbulent flows over landscapes with multi-scale microtopography. Earth Surface Dynamics 4:391–405

Poggi D, Katul G, Albertson J, Ridolfi L (2007) An experimental investigation of turbulent flows over a hilly surface. Phys Fluids 19:036,601

Rasmussen KR, Iversen JD, Rautaheimo P (1996) Saltation and wind flow interaction in a variable slope wind tunnel. Geomorphology 17:19–28

Rubin DM, Hunter RE (1987) Bedform alignment in directionally varying flows. Science 237:276–278

Runyon K, Bridges N, Ayoub F, Newman C, Quade J (2017) An integrated model for dune morphology and sand fluxes on mars. Earth Planet Sci Lett 457:204–212

Seidel DJ, Zhang Y, Beljaars A, Golaz JC, Jacobson AR, Medeiros B (2012) Climatology of the planetary boundary layer over the continental united states and europe. J Geophys Research 117:D17,106

Shao Y (2008) Physics and modelling of wind erosion, vol 37. Springer Science & Business Media

Shen Y, Zhang C, Huang X, Wang X, Cen S (2019) The effect of wind speed averaging time on sand transport estimates. Catena 175:286–293

Sheridan PF, Vosper SB (2006) A flow regime diagram for forecasting lee waves, rotors and downslope winds. Meteorological Applications 13:179–195

Sherman DJ, Farrell EJ (2008) Aerodynamic roughness lengths over movable beds: Comparison of wind tunnel and field data. J Geophys Res 113:1–10

Sherman DJ, Li B (2012) Predicting aeolian sand transport rates: A reevaluation of models. Aeolian Res 3:371–378

Smith AB, Jackson DWT, Cooper JAG (2017) Three-dimensional airflow and sediment transport patterns over barchan dunes. Geomorphology 278:28–42

Song Q, Gao X, Lei J, Li S (2019) Spatial distribution of sand dunes and their relationship with fluvial systems on the southern margin of the taklimakan desert, china. Geomatics, Natural Hazards and Risk 10:2408–2428

Spalding DB (1961) A single formula for the law of the wall. J Applied Mech 28:455–458

Stull R (2006) 9 - the atmospheric boundary layer. In: Wallace JM, Hobbs PV (eds) Atmospheric Science (Second Edition), second edition edn, Academic Press, San Diego, pp 375–417

Stull RB (1988) An introduction to boundary layer meteorology, vol 13. Springer Science & Business Media

Sullivan PP, McWilliams JC (2010) Dynamics of winds and currents coupled to surface waves. Annu Rev Fluid Mech 42:19–42

Sykes RI (1980) An asymptotic theory of incompressible turbulent boundary-layer flow over a small hump. J Fluid Mech 101:647–670

Taylor P, Teunissen H (1987) The Askervein hill project: overview and background data. Boundary-layer Meteorol 39:15–39

Taylor P, Mason P, Bradley E (1987) Boundary-layer flow over low hills. Boundary-layer Meteorol 39:107–132

Ungar JE, Haff PK (1987) Steady state saltation in air. Sedimentology 34:289–299

Unsworth C, Parsons D, Hardy R, Reesink A, Best J, Ashworth P, Keevil G (2018) The impact of nonequilibrium flow on the structure of turbulence over river dunes. Water Resour Res 54:6566–6584

Uppala SM, Kållberg P, Simmons AJ, Andrae U, Bechtold VDC, Fiorino M, Gibson J, Haseler J, Hernandez A, Kelly G, et al. (2005) The era-40 re-analysis. Q J R Meteorol Soc 131:2961–3012

Valance A, Rasmussen K, Ould El Moctar A, Dupont P (2015) The physics of aeolian sand transport. C R Physique 16:1–13

Virtanen P, Gommers R, Oliphant TE, Haberland M, Reddy T, Cournapeau D, Burovski E, Peterson P, Weckesser W, Bright J, et al. (2020) Scipy 1.0: fundamental algorithms for scientific computing in python. Nature methods 17:261–272

Vogelezang D, Holtslag A (1996) Evaluation and model impacts of alternative boundary-layer height formulations. Boundary-layer Meteorol 81:245–269

Vosper SB (2004) Inversion effects on mountain lee waves. Q J R Meteorol Soc 130:1723–1748

Walker I, Davidson-Arnott R, Bauer B, Hesp P, Delgado-Fernandez I, Ollerhead J, Smyth T (2017) Scale-dependent perspectives on the geomorphology and evolution of beach-dune systems. Earth-Science Rev 171:220–253

Walker IJ, Hesp PA, Davidson-Arnott RG, Bauer BO, Namikas SL, Ollerhead J (2009) Responses of three-dimensional flow to variations in the angle of incident wind and profile form of dunes: Greenwich dunes, prince edward island, canada. Geomorphology 105:127–138

Zhang C, Li Q, Zhou N, Zhang J, Kang L, Shen Y, Jia W (2016) Field observations of wind profiles and sand fluxes above the windward slope of a sand dune before and after the establishment of semi-buried straw checkerboard barriers. Aeolian Research 20:59–70

Zilker DP, Hanratty TJ (1979) Influence of the amplitude of a solid wavy wall on a turbulent flow. part 2. separated flows. J Fluid Mech 90:257–271

Zilker DP, Cook GW, Hanratty TJ (1977) Influence of the amplitude of a solid wavy wall on a turbulent flow. part 1. non-separated flows. J Fluid Mech

82:29–51

Local wind regime induced by giant linear dunes — Supplementary Material —

C. Gadal* · P. Delorme · C. Narteau · G.F.S. Wiggs · M. Baddock · J.M. Nield · P. Claudin

* Institut de Mécanique des Fluides de Toulouse, Université de Toulouse Paul Sabatier, CNRS, Toulouse INP-ENSEEIHT, Toulouse, France.
cyril.gadal@imft.fr

1. Shear velocity and calibration of the hydrodynamical roughness

As the regionally predicted and locally measured velocities are available at different heights, we can not compare them directly. We then convert all velocities into shear velocities u_*, characteristic of the turbulent velocity profile (Spalding 1961; Stull 1988):

$$\frac{u(z)}{u_*} = \frac{1}{\kappa} \ln\left(\frac{z}{z_0}\right), \tag{15}$$

where z is the vertical coordinate, $\kappa = 0.4$ the von Kármán constant and z_0 the hydrodynamic roughness. Several field measurements of hydrodynamic roughnesses are available Here cite a few old/general papers on roughness. In the absence of sediment transport, it scales with the geometric features of the bed (Pelletier and Field 2016) too specific paper? other older papers?. When transport occurs, it rather typically scales with the thickness of the transport layer. For aeolian saltation, this is controlled by the altitude of Bagnold's focal point (Durán et al. 2011; Valance et al. 2015), which depends on the wind velocity and grain properties (Sherman and Farrell 2008; Zhang et al. 2016; Field and Pelletier 2018). Whether associated with geometric features or with sediment transport, its typical order of magnitude is the millimetre scale.

We do not have precise velocity vertical profiles to be able to deduce an accurate value of z_0 in the various environments of the meteorological stations (vegetated, arid, sandy). Our approach is to rather select the hydrodynamic roughness which allows for the best possible matching between the regionally predicted and locally measured winds, i.e. minimising the relative difference δ between the wind vectors of both datasets:

$$\delta = \frac{\sqrt{\langle \| \boldsymbol{u}_{*,\mathrm{era}} - \boldsymbol{u}_{*,\mathrm{station}} \|^2 \rangle}}{\sqrt{\langle \| \boldsymbol{u}_{*,\mathrm{era}} \| \rangle \langle \| \boldsymbol{u}_{*,\mathrm{station}} \| \rangle}}, \tag{16}$$

where $\langle . \rangle$ denotes time average. This parameter is computed for values of z_0 in ERA5-Land analysis ranging from 10^{-5} m to 10^{-2} m for the four different stations. Note that for the Deep Sea and South Namib stations, where the giant dunes feedback presumably affect the wind, we take into account the non-deflected winds only in the calculation of δ (with a 15° tolerance).

As shown in Suppl. Fig. S3, the minimum values of δ in the space (z_0^{ERA5Land}, z_0^{local}) form a line. We thus set the roughness in the ERA5-Land analysis to the typical value $z_0 = 10^{-3}$ m, and deduce the corresponding ones for the local stations. It leads to 2.7, 0.8, 0.1 and 0.5 mm for the Adamax, Deep Sea, Huab and South Namib stations, respectively. Importantly, this approach somewhat impacts the calculation of the shear velocities, but not that of the wind directions. As such, most of our conclusions are independent of such a choice. However, it may affect the magnitude of the wind velocity attenuation/amplification in flow confinement situations.

2. Computation of the ABL characteristics

The estimation of the non-dimensional numbers associated with the ABL requires the computation of representative meteorological quantities. In arid areas, the vertical structure of the atmosphere can be approximated by a well mixed convective boundary layer of height H, topped by the stratified free atmosphere (Stull 1988; Shao 2008). In this context, one usually introduces the virtual potential temperature T_{vp}, which is a constant T_0 inside the boundary layer, and increases linearly in the FA (Suppl. Fig. S9a):

$$T_{\mathrm{vp}}(z) = \begin{cases} T_0 & \text{for } z \leq H, \\ T_0 \left(1 + \dfrac{\Delta T_{\mathrm{vp}}}{T_0} + \dfrac{N^2}{g}(z - H)\right) & \text{for } z \geq H, \end{cases} \tag{17}$$

where ΔT_{vp} is the temperature discontinuity at the capping layer and $N = \sqrt{g\partial_z T_{\mathrm{vp}}/T_0}$ is the Brunt-Väisälä frequency, characteristic of the stratification. Note that, under the usual Boussinesq approximation, temperature and air density variations are simply related by $\delta T_{\mathrm{vp}}/T_0 \simeq -\delta\rho/\rho_0$ (see Suppl. Mat. of Andreotti et al. (2009)), so that N can equivalently be defined from the density gradient as next to Eq. 1.

The ERA5 dataset provides vertical profiles of the geopotential ϕ, the actual temperature T and the specific humidity η at given pressure levels P. The vertical coordinate is then calculated as:

$$z = \frac{\phi R_{\mathrm{t}}}{g R_{\mathrm{t}} - \phi}, \tag{18}$$

where $R_{\mathrm{t}} = 6371229$ m is the reference Earth radius and $g = 9.81$ m s^{-2} is the gravitational acceleration. One also computes the virtual potential temperature as:

$$T_{\mathrm{vp}} = T\left[1 + \left(\frac{M_d}{M_w} - 1\right)\eta\right]\left(\frac{P_0}{P}\right)^{R/C_p}, \tag{19}$$

where $P_0 = 10^5$ Pa is the standard pressure, $R = 8.31$ J/K is the ideal gas constant, $C_p \simeq 29.1$ J/K is the air molar heat capacity, and $M_w = 0.018$ kg/Mol and $M_d = 0.029$ kg/Mol are the molecular masses of water and dry air respectively. The specific humidity is related to the vapour pressure p_w as

$$\eta = \frac{\frac{M_w}{M_d} p_w}{p - \left(1 - \frac{M_w}{M_d}\right) p_w} \, . \tag{20}$$

The ERA5 dataset also provides an estimate of the ABL depth H, based on the behaviour of the Richardson vertical profile. This dimensionless number is defined as the ratio of buoyancy and flow shear terms, and can be expressed as $\mathrm{Ri} = N^2/(\partial_z u)^2$. It vanishes in the lower well-mixed layer where T_{vp} is constant, and increases in the stratified FA. Following the method and calibration of Vogelezang and Holtslag (1996); Seidel et al. (2012), the value $\mathrm{Ri}(z) \simeq 0.25$ has been shown to be a good empirical criterion to give $z \simeq H$ within a precision varying from 50% for the shallower ABL (e.g. at night) to 20% for situations of stronger convection.

Examples of vertical profiles of the virtual potential temperature deduced from ERA5 are shown in Suppl. Fig. S9a. For each of them, an average temperature is computed below the ABL depth ($z < H$), and a linear function is fitted above, allowing us to extract the temperature jump $\varDelta T_{\mathrm{vp}}$. Importantly, some profiles display a vertical structure that cannot be approximated by the simple form (17) used here (Suppl. Fig. S9b). In practice, we removed from the analysis all of those leading to the unphysical case $\varDelta T_{\mathrm{vp}} < 0$. We have noticed that these 'ill-processed' profiles dominantly occur in winter and are evenly spread across the hours of the day. Importantly, they represent $\simeq 12\%$ of the data only (Suppl. Fig. S9c,d), and we are thus confident that this data treatment does not affect our conclusions.

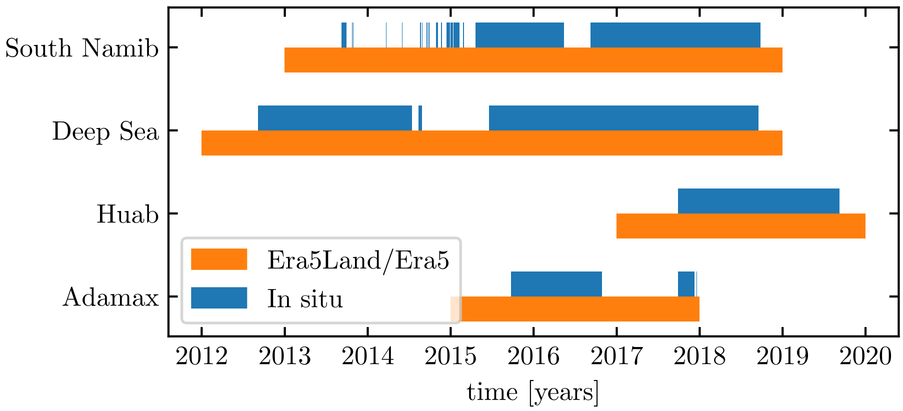

Fig. S1 Gant chart representing the valid time steps for the two data sets, for all stations.

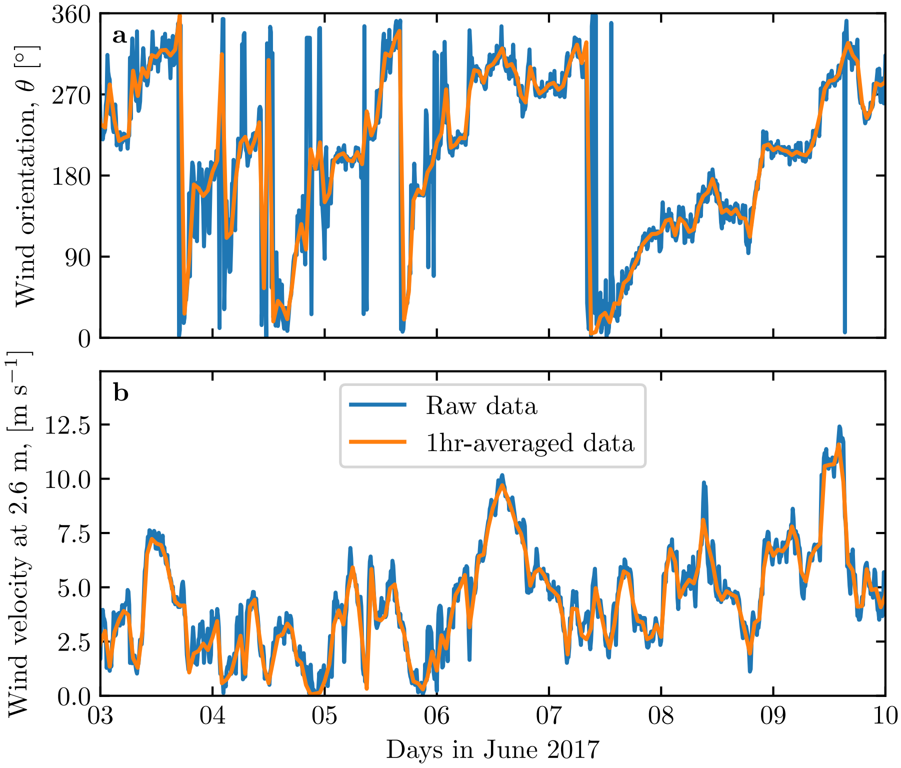

Fig. S2 Comparison between raw local wind measurements, and hourly-averaged data for South Namib station. **a**: wind direction. **b**: wind velocity at height 2.6 m.

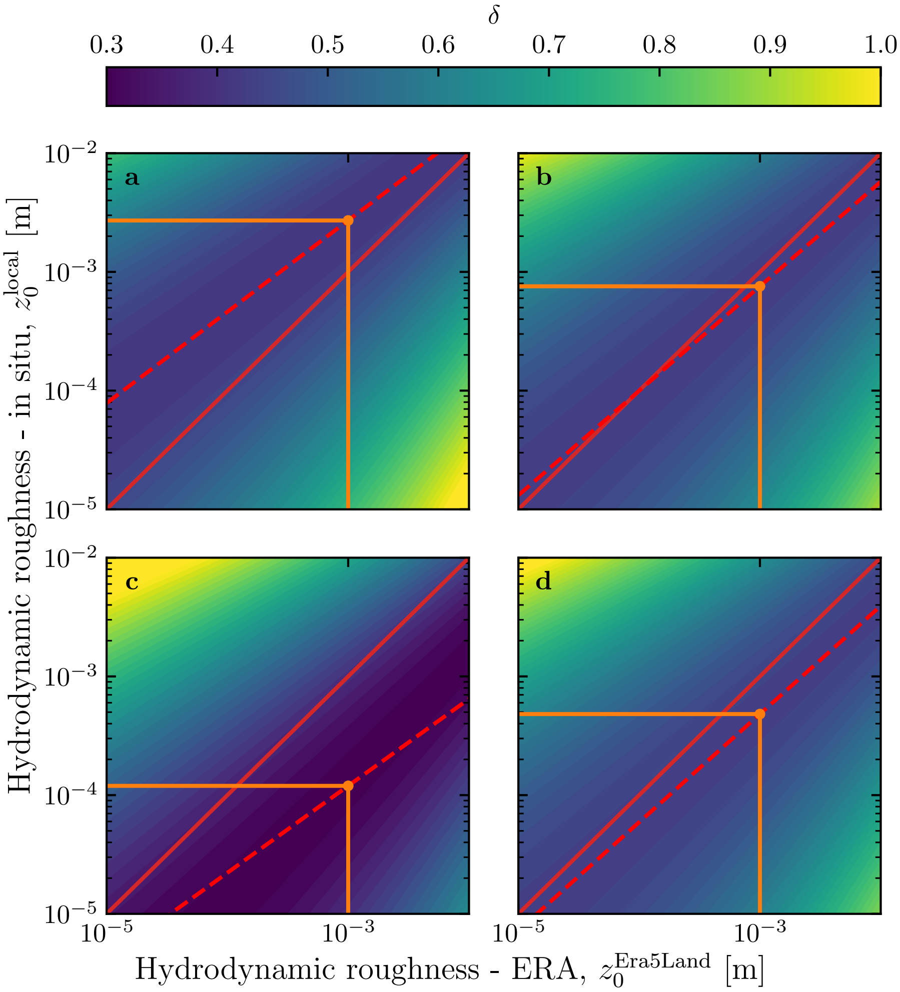

Fig. S3 Calibration of hydrodynamic roughness. The parameter δ (Eq. 16) quantifying the difference between local and predicted winds is shown in colorscale as a function of the hydrodynamic roughnesses chosen for the ERA5-Land and for local winds, for the (**a**) Adamax, (**b**) Deep Sea, (**c**) Huab and (**d**) South Namib stations. The red dashed and plain lines shows the minima of δ and the identity line, respectively. The orange lines and dots highlight the chosen hydrodynamic roughnesses for the local winds deduced from setting $z_0^{\mathrm{ERA5Land}} = 1$ mm.

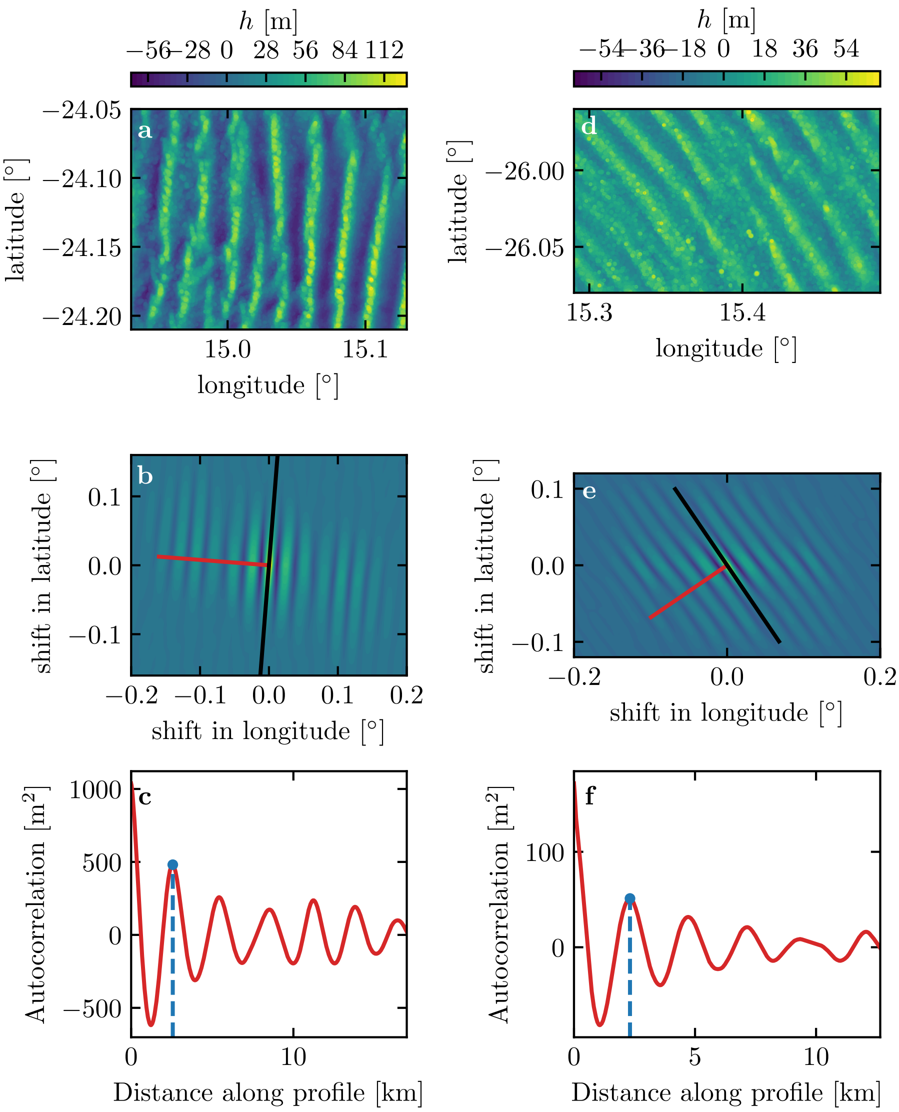

Fig. S4 Analysis of the DEMs of the Deep Sea (left column – panels **a**, **b**, **c**) and South Namib (right column – panels **d**, **e**, **f**) stations. **a-d**: Bed elevation detrended by a fitted second order polynomial base-line. **b-e**: Autocorrelation matrix shown in colorscale. The black line shows the detected dune orientation, and the red line represents the autocorrelation profile along which the dune wavelength is calculated, displayed in **c-f**. The blue lines and dots show the first peak of the autocorrelation profile, whose abscissa gives the characteristic wavelength of the dune pattern.

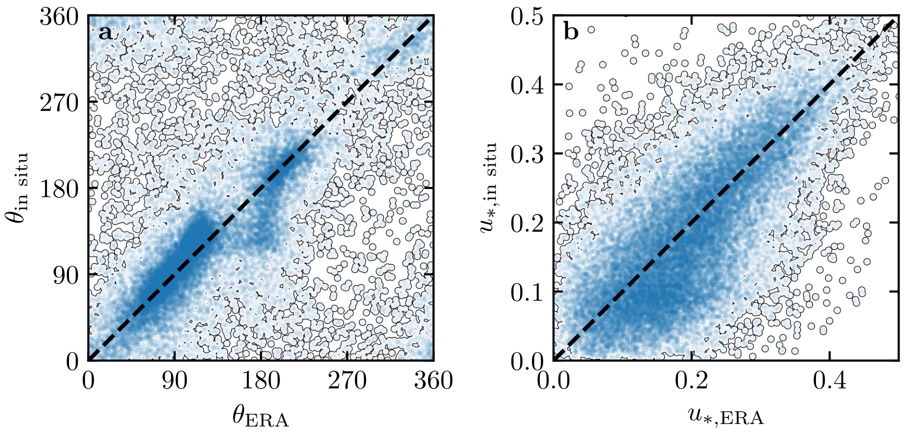

Fig. S5 Statistical comparison of the wind orientation (**a**) and velocity (**b**) between the ERA5-Land dataset and the local measurements for the Huab and Adamax stations. Data point clustering around identity lines (dashed and black) provide evidence for agreement of the two sets.

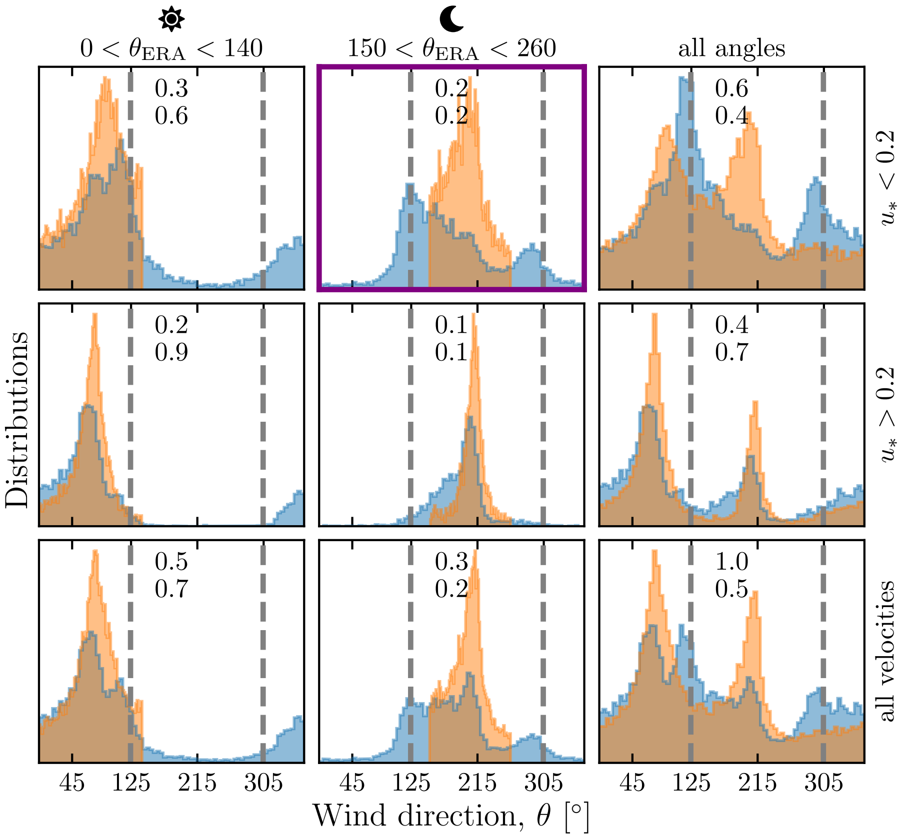

Fig. S6 Distributions of wind direction at the South Namib Station for the ERA5-Land climate reanalysis (orange) and the local measurements (blue) – equivalent of Fig. 3. In each subplot, both distributions are plotted from the same time steps, selected with constraints on the wind direction (columns) and/or wind velocity (rows) in the ERA5-Land dataset. The gray vertical dashed lines indicate the dune orientation. The numbers at the top centre give the percentage of time steps selected in each sub-range, as well as the percentage of them corresponding to the day (between 1000 UTC and 2200 UTC). The purple frame highlights the regime (small wind velocities, nocturnal summer wind) during which the wind data from both datasets differ.

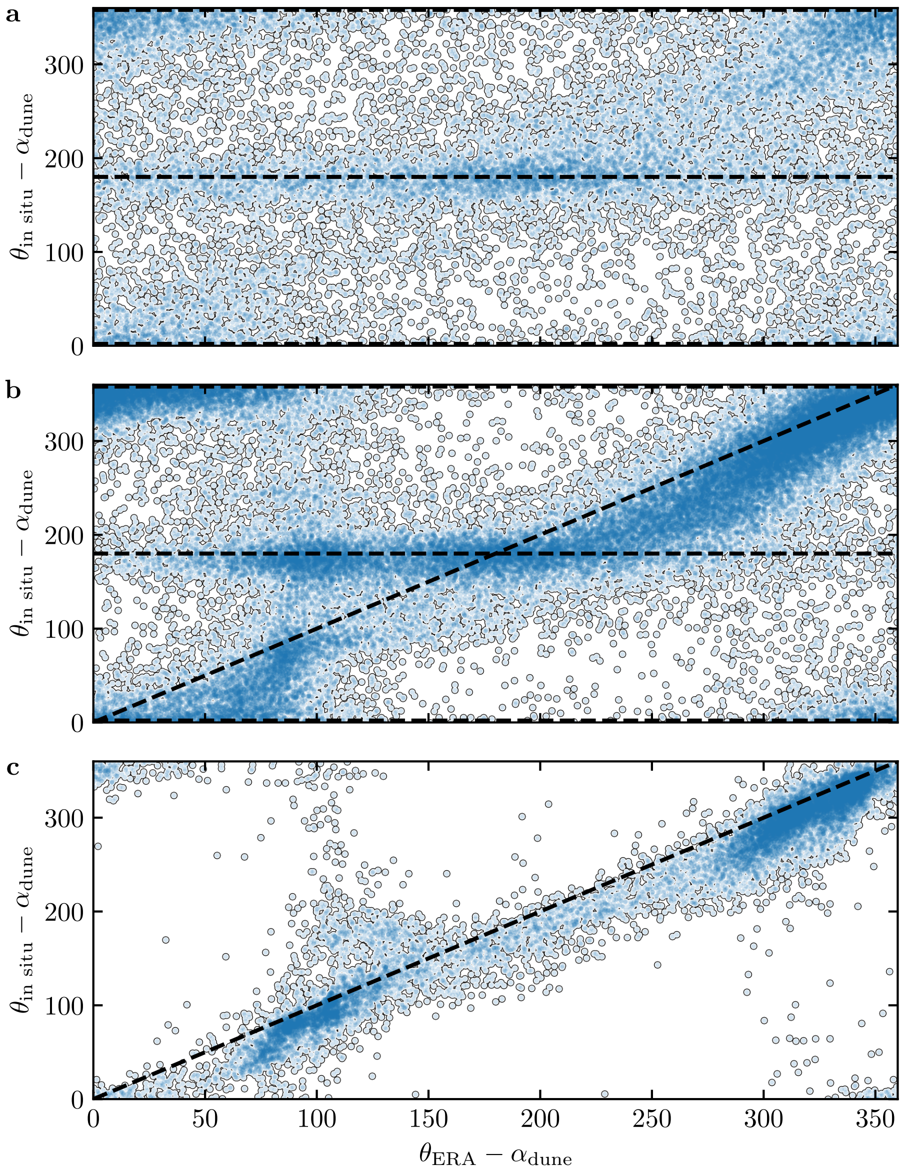

Fig. S7 Statistical comparison of the wind orientation between the ERA5-Land dataset and the local measurements for the South Namib and Deep Sea stations, for different velocity ranges. **a**: $u_{*,\mathrm{ERA}} < 0.1$ m s^{-1}. **b**: $0.1 < u_{*,\mathrm{ERA}} \leq 0.25$ m s^{-1}. **c**: $u_{*,\mathrm{ERA}} \geq 0.25$ m s^{-1}. The measured dune orientations are subtracted to the wind orientation, which allows us to plot both stations on the same graph. Black dashed lines indicate locally measured orientations aligned with the dune crests (here 0°, 180° and 360° – panels **a**, **b**), as well as the identity lines (panels **b**, **c**).

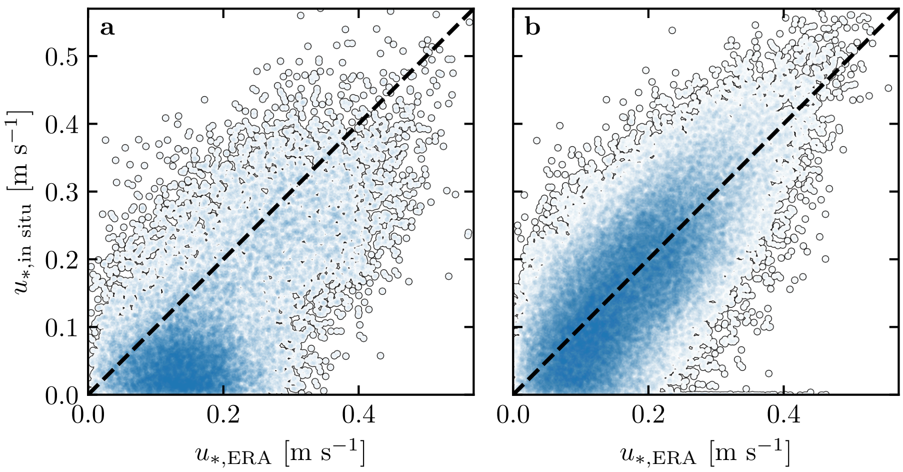

Fig. S8 Statistical comparison of the wind velocity between the ERA5-Land dataset and the local measurements for the South Namib and Deep Sea stations. **a**: Nocturnal summer easterly wind. **b**: Diurnal southerly wind. Black dashed lines are identity lines. The angle ranges used to select diurnal and nocturnal summer winds are the same as those in Fig. 3 and Suppl. Fig. S6.

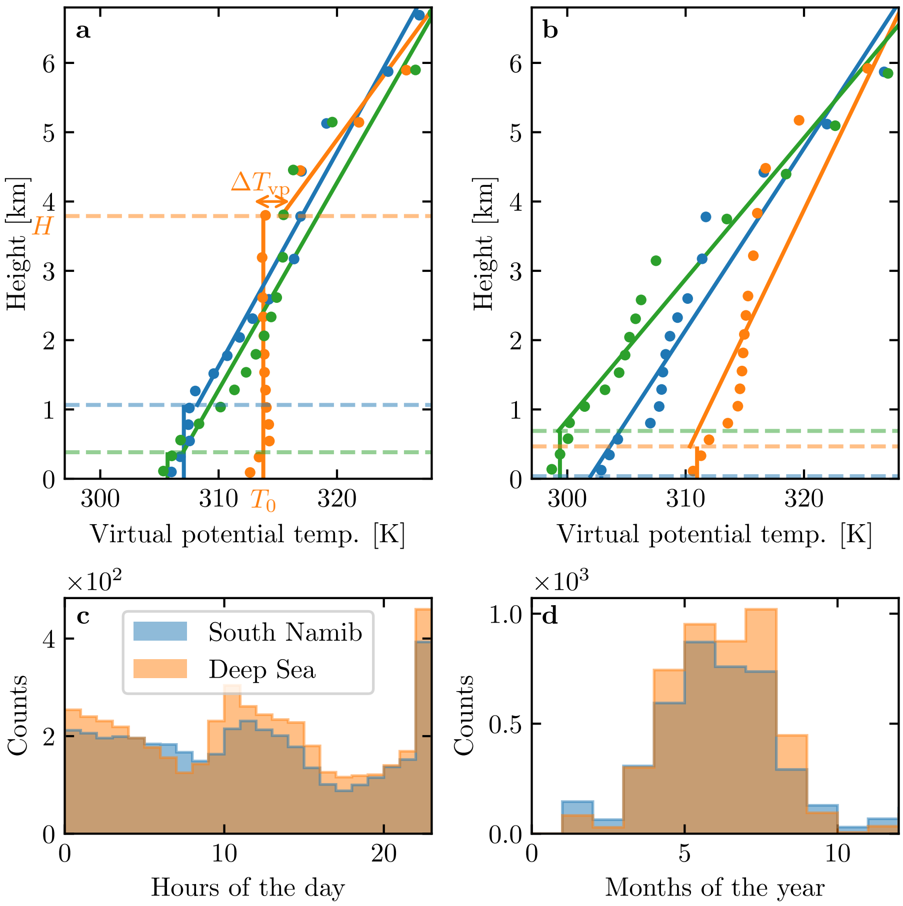

Fig. S9 **a**: Vertical profiles of the virtual potential temperature at three different times (blue: 29/11/2012 - 1100 UTC, orange: 21/03/2017 - 1200 UTC, green: 21/03/2017 - 2000 UTC) at the South Namib station. Dots: data from the ERA5 reanalysis. Dashed lines: boundary layer height given by the ERA5 reanalysis. Plain lines: vertical (ABL) and linear (FA) fits to estimate the quantities displayed in Suppl. Fig. S10. **b**: Examples of ill-processed vertical profiles at three different times (blue: 2/12/2013 - 2300 UTC, orange: 20/03/2017 - 0000 UTC, green: 14/07/2017 - 1400 UTC) at the South Namib station. **c**: Hourly distribution of ill-processed vertical profiles. **d**: Monthly distribution of ill-processed vertical profiles.

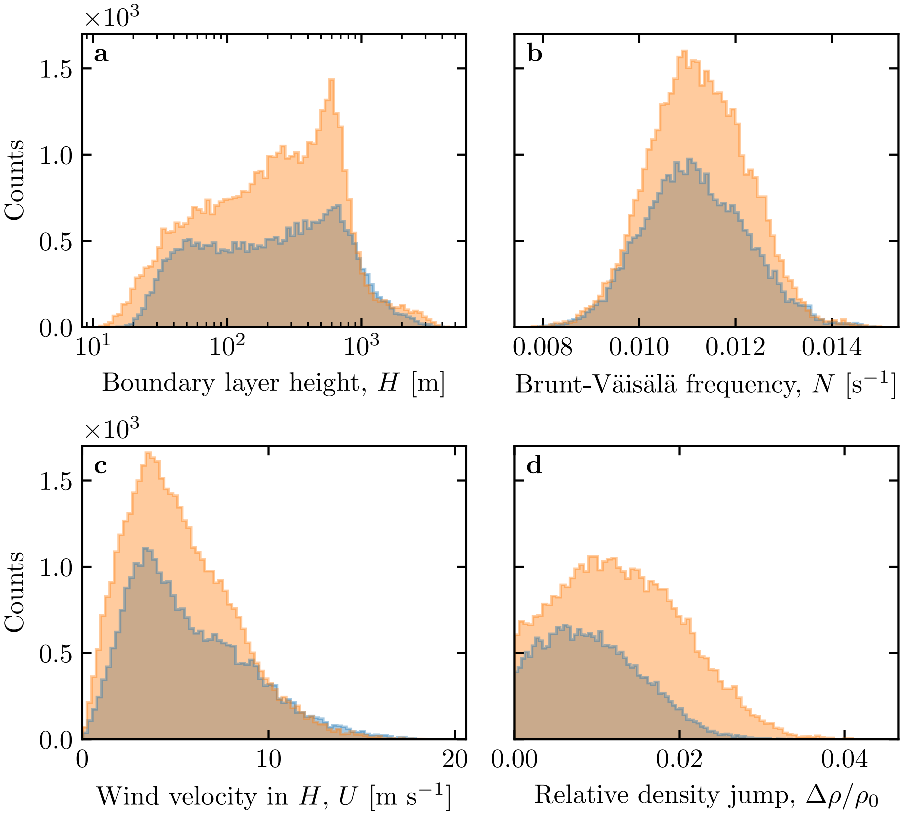

Fig. S10 Distributions of the meteorological parameters resulting from the processing of the ERA5-Land data for the South Namib (blue) and the Deep Sea (orange) stations. axis label : panel c -velocity at (height) H. Is this for all day/night/seasons ?

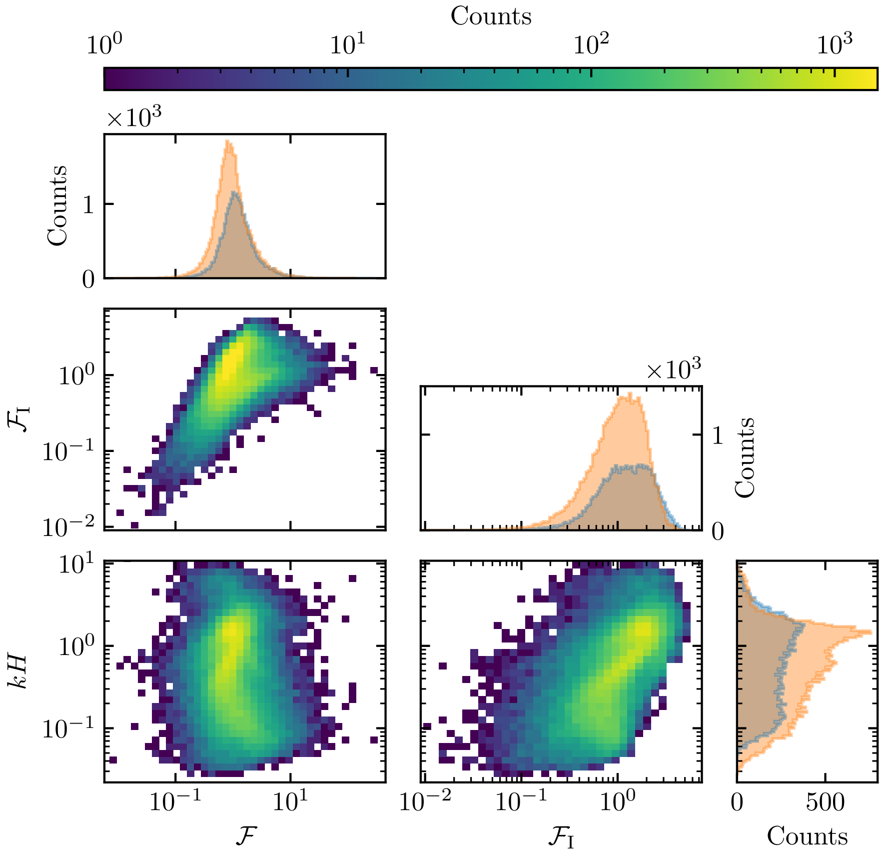

Fig. S11 Non-dimensional parameters distributions. For the marginal ??? distributions, the orange correspond to the South Namib station, and the blue to the Deep Sea station.

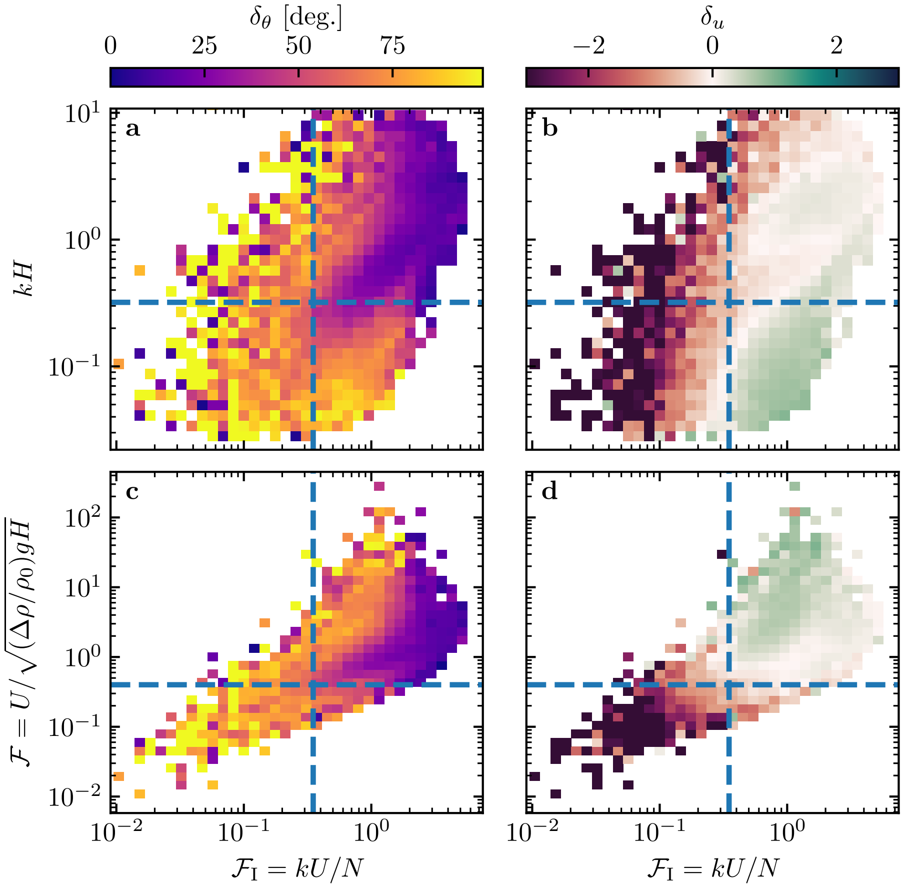

Fig. S12 Regime diagrams of the wind deviation δ_θ and relative attenuation/amplification δ_u in the spaces ($\mathcal{F}_\mathrm{I}$, kH) and ($\mathcal{F}_\mathrm{I}$, $\mathcal{F}$), containing the data from both the Deep Sea and South Namib stations. Blue dashed lines empirically delimit the different regimes. The point density in each bin of the diagrams is shown in Suppl. Fig. S11. The similar regime diagrams in the space ($\mathcal{F}$, kH) are shown in Fig. 5.

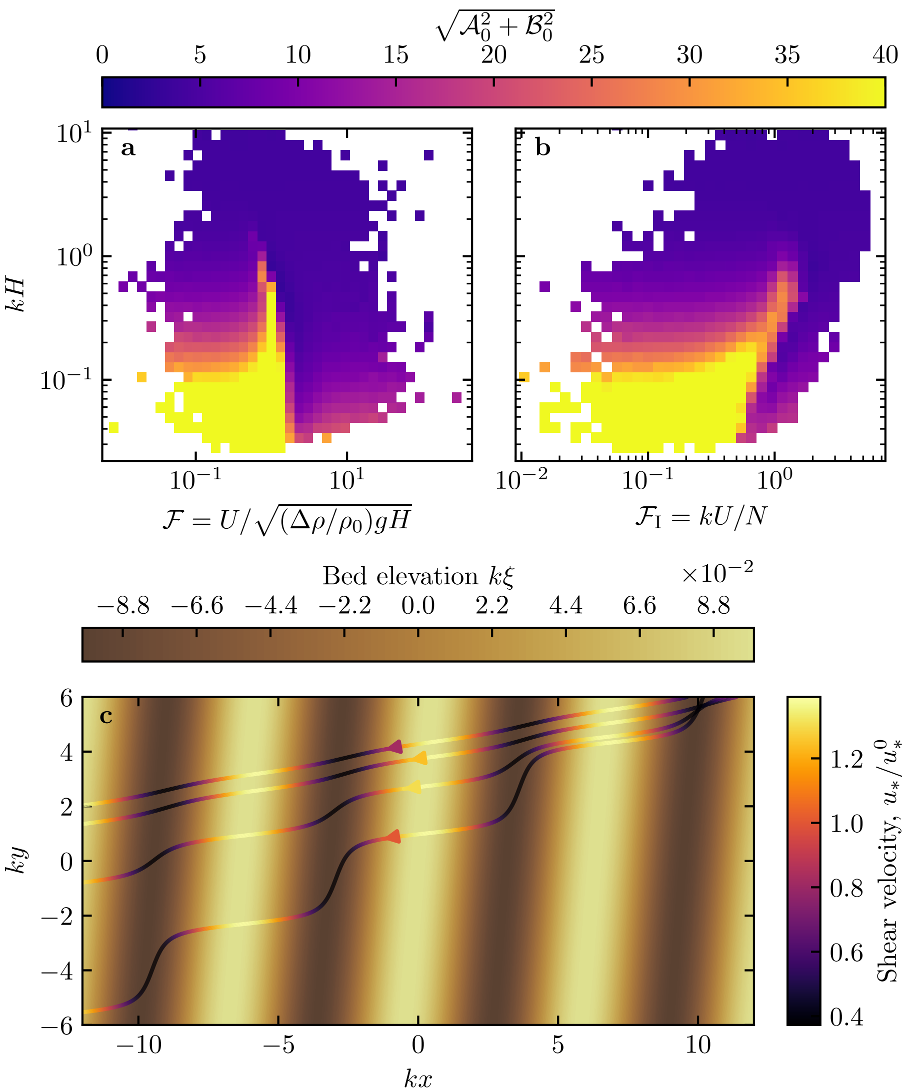

Fig. S13 Computation of the flow disturbance with the linear model of Andreotti et al. (2009). (a) and (b) Magnitude of the hydrodynamic coefficients $\mathcal{A}_0$ and $\mathcal{B}_0$, calculated from the values of the non-dimensional numbers corresponding to the ERA5-Land time series presented in Figs. 4 and 5. (c) Shear velocity streamlines over sinusoidal ridges of amplitude $k\xi_0 = 0.1$ and for increasing values of $\sqrt{\mathcal{A}_0^2+\mathcal{B}_0^2}$. From the upper to the lower streamline, values of $\left(kH,\ \mathcal{F},\ \mathcal{F}_\mathrm{I},\ \mathcal{A}_0,\ \mathcal{B}_0,\ \sqrt{\mathcal{A}_0^2+\mathcal{B}_0^2}\right)$ are (1.9, 0.6, 1.5, 3.4, 1.0, 3.5), (1.5, 0.3, 0.4, 4.8, 1.4, 5.0), (0.1, 3.5, 1.0, 8.6, 0.1, 8.6), (0.5, 0.05, 0.04, 9.6, 2.5, 9.9).